

UNIVERSIDADE FEDERAL DE UBERLÂNDIA

Thiago Rezende de Castro

Numerical Simulations of High-lift Configurations on a NACA4412 Airfoil

Uberlândia

2024

Thiago Rezende de Castro

Numerical Simulations of High-lift Configurations on a NACA4412 Airfoil

Final thesis for the graduation course of Aeronautical Engineering of the Universidade Federal de Uberlândia for the degree of Bachelor in Aeronautical Engineering.
Supervisor: Prof. Dr. Odenir de Almeida

Uberlândia
2024

Thiago Rezende de Castro

Numerical Simulations of High-lift Configurations on a NACA4412 Airfoil

This final thesis has been considered suitable for obtaining the Bachelor's Degree in Aeronautical Engineering and approved in its final form by the Aeronautical Engineering Graduate Course.

Uberlândia, August 16, 2024.

Reviewing Board:

Prof. Dr. Odenir de Almeida
Universidade Federal de Uberlândia

Dr. Luiz Paulo Borges Miranda
Universidade Federal de Uberlândia

Prof. Dr. João Rodrigo Andrade
Universidade Federal de Uberlândia

ACKNOWLEDGEMENTS

I would like to express my gratitude to all those who have contributed in some way to this work. Prof. Dr. Odenir de Almeida, for his valuable guidance, patience and trust throughout the process. As well as my former advisor and friend, Dr. Luiz Paulo Borges Miranda, who introduced me to the world of Computational Fluid Dynamics and sparked an interest I didn't know I had.

To my family, especially my parents, Telesmar and Isabella, I thank you for your unconditional support and for always believing in my potential. To my friends and especially my boyfriend, Gabriel, who have shared moments of anxiety but also of joy, my sincere gratitude for their companionship and emotional support over all these years.

Gostaria de expressar minha gratidão a todos aqueles que, de alguma forma, contribuíram para a realização deste trabalho. Prof. Dr. Odenir de Almeida, por sua orientação valiosa, paciência e confiança ao longo de todo o processo. Assim como ao meu antigo orientador, Dr. Luiz Paulo Borges Miranda, que me apresentou ao mundo da simulação numérica de fluidos e me instigou o interesse que não sabia que possuía.

À minha família, especialmente aos meus pais, Telesmar e Isabella, agradeço pelo apoio incondicional e por sempre acreditarem no meu potencial. Aos meus amigos e principalmente ao meu namorado, Gabriel, que compartilharam momentos de ansiedade, mas também de alegria, minha sincera gratidão pelo companheirismo e apoio emocional durante todos esses anos.

ABSTRACT

This work addresses the numerical simulation of high-lift systems in the aeronautical industry. The main objective was to evaluate the performance of different configurations of such high-lift devices, identifying their advantages and disadvantages. The secondary objective was to develop a robust numerical method for simulating flows around airfoils, using the OpenFOAM software. Numerical analyses were carried out on five different configurations — namely, the plain flap, split flap, slotted flap, Fowler flap and Junkers flap — under similar conditions, allowing for a consistent comparison of outcomes. All flaps were deflected by 10° and analyzed at a Reynolds of $1.7 \cdot 10^5$ over a range of angles of attack between -4° and 16°. The Spallart-Almarras turbulence model was used in all simulations, which were carried out in the steady state. Quantitative results were analyzed for the coefficients of lift (C_l) and drag (C_d) per unit length and the coefficient of pressure (C_p) on the surfaces of the airfoils analyzed, as well as the velocity and pressure fields of the flows.

To check the quality of the simulation, the method was used to replicate experimental and numerical results obtained by other authors for the flow around airfoils (flapped or not). In addition, the convergence of the simulation between successively refined meshes and the quality of the boundary layer modeling from the dimensionless parameter y^+ were analyzed, and both obtained good results with residual errors in the order of 10^{-5}. The results obtained show the efficiency and robustness of the proposed method and its applicability in different scenarios. It was found that the simulations presented reliable and coherent results for lift and drag generation, but for angles of attack close to stall, convergence was more difficult. In addition, it was possible to identify the superiority in lift generation of the flap configurations most commonly used in the aeronautical industry, such as the slotted flap and the Fowler flap.

Keywords: Numerical simulation; OpenFOAM; High-lift devices; Flaps.

LIST OF FIGURES

Figure 1 – Different high-lift configurations 11
Figure 2 – Diamond DA42 Twin Star as an example of an aircraft with plain flaps. 12
Figure 3 – Supermarine Spitfire as an example of an aircraft with split flaps. . . . 13
Figure 4 – Cessna 172 Skyhawk as an example of an aircraft with slotted flaps. . . 13
Figure 5 – Boeing 747 as an example of an aircraft with fowler flaps. 14
Figure 6 – Junkers 52 as an example of an aircraft with junkers flaps. 15
Figure 7 – Experimental visualization conducted by Osborne Reynolds 21
Figure 8 – Mean velocity in function of wall distance 23
Figure 9 – Background mesh generated by *blockMesh*, showing (a) whole computational domain and (b) zoomed origin region. 26
Figure 10 – Mesh generated by *snappyHexMesh*, showing (a) the refinement region near the airfoil, (b) zoomed transiotion layers and (c) farfield region. . 27
Figure 11 – (a) Lift and (b) Drag coefficients results obtained in the present work and by Ladson (1988) 31
Figure 12 – (a) Lift and (b) Drag coefficients results obtained in the present work and by Jawahar et al. (2018) 32
Figure 13 – Wake velocity profiles at obtained (a) in the present work and (b) by Jawahar et al. (2018) for $\delta = 5°$ e $\alpha = 0°$. 33
Figure 14 – Pressure coefficient distribution over the flapped airfoil obtained (a) in the present work and (b) by Jawahar et al. (2018) for $\delta = 10°$ e $\alpha = 4°$. 34
Figure 15 – (a) Lift and (b) Drag coefficients results obtained in the present work and by Kumar and Kumar (2013) 35
Figure 16 – y^+ distribution along various airfoil and high-lift surfaces. 36
Figure 17 – Influence of mesh refinement in lift and drag coefficients for (a), (b) the clean airfoil and (c), (d) the plain flap. 37
Figure 18 – (a) Lift and (b) Drag coefficients results for the clean airfoil and different flap configurations as a function of the angle of attack. (c) Lift coefficient as a function of Drag coefficient. 38
Figure 19 – Velocity field of the flow over the clean airfoil for (a) $\alpha = 0°$, (b) $\alpha = 4°$, (c) $\alpha = 8°$, (d) $\alpha = 12°$ and (e) $\alpha = 14°$. 39
Figure 20 – Kinematic pressure field of the flow over the clean airfoil for (a) $\alpha = 0°$, (b) $\alpha = 4°$, (c) $\alpha = 8°$, (d) $\alpha = 12°$ and (e) $\alpha = 14°$. 40
Figure 21 – Pressure coefficient distribution along the clean airfoil for (a) $\alpha = 0°$, (b) $\alpha = 4°$, (c) $\alpha = 8°$, (d) $\alpha = 12°$ and (e) $\alpha = 16°$. 41
Figure 22 – Velocity field of the flow over the airfoil with plain flap for (a) $\alpha = 0°$, (b) $\alpha = 4°$, (c) $\alpha = 8°$, (d) $\alpha = 13°$ and (e) $\alpha = 14°$. 42

Figure 23 – Kinematic pressure field of the flow over the airfoil with plain flap for (a) $\alpha = 0°$, (b) $\alpha = 4°$, (c) $\alpha = 8°$, (d) $\alpha = 13°$ and (e) $\alpha = 14°$. 43
Figure 24 – Pressure coefficient distribution along the airfoil with plain flap for (a) $\alpha = 0°$, (b) $\alpha = 4°$, (c) $\alpha = 8°$, (d) $\alpha = 13°$ and (e) $\alpha = 14°$. 44
Figure 25 – Velocity field of the flow over the airfoil with split flap for (a) $\alpha = 0°$, (b) $\alpha = 4°$, (c) $\alpha = 8°$, (d) $\alpha = 12°$ and (e) $\alpha = 15°$. 45
Figure 26 – Kinematic pressure field of the flow over the airfoil with split flap for (a) $\alpha = 0°$, (b) $\alpha = 4°$, (c) $\alpha = 8°$, (d) $\alpha = 12°$ and (e) $\alpha = 15°$. 46
Figure 27 – Pressure coefficient distribution along the airfoil with split flap for (a) $\alpha = 0°$, (b) $\alpha = 4°$, (c) $\alpha = 8°$, (d) $\alpha = 13°$ and (e) $\alpha = 14°$. 47
Figure 28 – Velocity field of the flow over the airfoil with slotted flap for (a) $\alpha = 0°$, (b) $\alpha = 4°$, (c) $\alpha = 8°$, (d) $\alpha = 12°$ and (e) $\alpha = 16°$. 48
Figure 29 – Kinematic pressure field of the flow over the airfoil with slotted flap for (a) $\alpha = 0°$, (b) $\alpha = 4°$, (c) $\alpha = 8°$, (d) $\alpha = 12°$ and (e) $\alpha = 16°$. 49
Figure 30 – Pressure coefficient distribution along the airfoil with slotted flap for (a) $\alpha = 0°$, (b) $\alpha = 4°$, (c) $\alpha = 8°$, (d) $\alpha = 13°$ and (e) $\alpha = 14°$. 50
Figure 31 – Velocity field of the flow over the airfoil with fowler flap for (a) $\alpha = 0°$, (b) $\alpha = 4°$, (c) $\alpha = 8°$, (d) $\alpha = 13°$ and (e) $\alpha = 14°$. 51
Figure 32 – Kinematic pressure field of the flow over the airfoil with fowler flap for (a) $\alpha = 0°$, (b) $\alpha = 4°$, (c) $\alpha = 8°$, (d) $\alpha = 13°$ and (e) $\alpha = 14°$. 52
Figure 33 – Pressure coefficient distribution along the airfoil with fowler flap for (a) $\alpha = 0°$, (b) $\alpha = 4°$, (c) $\alpha = 8°$, (d) $\alpha = 13°$ and (e) $\alpha = 14°$. 53
Figure 34 – (a) Lift and (b) Drag coefficients results for the clean airfoil and both positions of the Junkers flap as a function of the angle of attack. 54
Figure 35 – Velocity field of the flow over the airfoil with Junkers flap in resting position for (a) $\alpha = 0°$, (b) $\alpha = 4°$, (c) $\alpha = 8°$, (d) $\alpha = 13°$ and (e) $\alpha = 14°$. 55
Figure 36 – Velocity field of the flow over the airfoil with Junkers flap for (a) $\alpha = 0°$, (b) $\alpha = 4°$, (c) $\alpha = 8°$, (d) $\alpha = 13°$ and (e) $\alpha = 14°$. 56
Figure 37 – Kinematic pressure field of the flow over the airfoil with Junkers flap in resting position for (a) $\alpha = 0°$, (b) $\alpha = 4°$, (c) $\alpha = 8°$, (d) $\alpha = 13°$ and (e) $\alpha = 14°$. 57
Figure 38 – Kinematic pressure field of the flow over the airfoil with Junkers flap for (a) $\alpha = 0°$, (b) $\alpha = 4°$, (c) $\alpha = 8°$, (d) $\alpha = 13°$ and (e) $\alpha = 14°$. . . 58
Figure 39 – Pressure coefficient distribution along the airfoil with Junkers flap for (a) $\alpha = 0°$, (b) $\alpha = 4°$, (c) $\alpha = 8°$, (d) $\alpha = 13°$ and (e) $\alpha = 14°$. 59

CONTENTS

1 INTRODUCTION AND LITERATURE REVIEW 8
1.1 MOTIVATION 8
1.2 LITERATURE REVIEW 9
2 HIGH-LIFT DEVICES 11
2.1 PLAIN FLAP 12
2.2 SPLIT FLAP 12
2.3 SLOTTED FLAP 13
2.4 FOWLER FLAP 14
2.5 JUNKERS FLAP 15
3 COMPUTATIONAL FLUID DYNAMICS (CFD) 16
3.1 OPENFOAM® 17
4 NUMERICAL METHODOLOGY 19
4.1 SOLVERS 19
4.1.1 simpleFoam 19
4.2 TURBULENCE MODEL 21
4.2.1 Mesh requirements 22
4.2.2 RAS 23
5 PREPROCESSING 25
5.1 MESH GENERATION 25
5.1.1 *blockMesh* 25
5.1.2 *snappyHexMesh* 26
5.2 BOUNDARY CONDITIONS 28
6 POSTPROCESSING 29
7 LITERATURE COMPARISON 31
7.1 LADSON (1988) 31
7.2 JAWAHAR ET AL. (2018) 32
7.3 KUMAR AND KUMAR (2013) 34
8 RESULTS 36
8.1 MESH REFINEMENT TEST 36
8.2 HIGH-LIFT CONFIGURATION COMPARISON 38
8.2.1 Plain flap 41
8.2.2 Split flap 44
8.2.3 Slotted flap 48
8.2.4 Fowler flap 51
8.2.5 Junkers flap 54
9 CONCLUSIONS 60
REFERENCES 61

1 INTRODUCTION AND LITERATURE REVIEW

1.1 MOTIVATION

In the last decade, aeronautical technology has advanced significantly towards lighter and more efficient aircraft designs and a large part of this is due to high-lift devices. Small improvements in the aerodynamic performance of these systems can lead to major benefits in terms of aircraft weight and performance. For example, according to Meredith (1993), an increase of just 1% in the maximum lift coefficient of a commercial jet aircraft allows for the allocation of approximately 22 additional passengers or 2000 kg of payload. This substantial impact during different flight stages has sparked an increasing interest within the aviation industry. According to van Dam (2002), the presence of high-lift devices is crucial for the competitiveness of commercial jet aircrafts in terms of aerodynamic efficiency during cruise, especially considering that laminar flow technology on aerodynamic surfaces is not yet widespread. According to the author, high-lift systems will continue to be a necessity for the foreseeable future.

For long enough, the aeronautical industry has relied on experimental wind tunnel analyses for the design of wings and high-lift surfaces. However, with the increasing geometry complexity and the emergence of new techniques to improve aerodynamic efficiency, this type of approach is no longer the best option. Despite their advantages, these procedures are time-consuming and costly, as well as the fact that they introduce errors and uncertainties associated with the experiments that need to be addressed. In addition, the flow around aircraft surfaces is intrinsically non-linear and unstable, which requires more advanced approaches. To address these complexities, Computational Fluid Dynamics (CFD) and optimization algorithms have become key tools in aeronautical design, enabling faster and more cost-effective analyses. With the continued advancement of these technologies, including the introduction of supercomputers, even more significant improvements are expected.

Despite its advantages, the use of CFD to analyze aerodynamic flows still presents difficulties to overcome. For simulations at low Reynolds numbers, the transition of the boundary layer is a problem and requires suitable and specialized turbulence models; in other cases, the presence of recirculation zones, re-attachment and adverse pressure gradients can make it difficult to solve the constituent equations. The mesh used must be adequate to capture the behavior of the fluid in the boundary layer and in the small gaps that some of the configurations of high-lift devices have, but at the same time it must be sufficiently large so that the boundary conditions of the computational domain do not affect the results.

It will be clear from the analysis of the literature presented below that a large amount of literature addressing the numerical simulation of high-lift devices can be found,

but it is difficult to compare results from different configurations as numerical analyses are often performed on different geometries and Reynolds numbers. To contribute to the literature, this work seeks to compile numerical analyses of different configurations of high-lift devices under similar conditions using the OpenFOAM software, while creating a robust numerical method for simulating flow around airfoils in general. An open source software was chosen as it makes it easier for other authors to replicate the results found in this work, as well as being accessible to members of academia.

1.2 LITERATURE REVIEW

In the literature one can find several examples of the use of CFD in the design and analysis of various types of high-lift devices. For example, Bhandari (2019), Kumar and Kumar (2013) and Fonseca et al. (2019) all numerically analyzed the flow around an airfoil equipped with a plain flap for low Reynolds numbers (around 10^5). While the first two papers analyzed the NACA 0012 airfoil using Ansys Fluent software, the latter repeated their analysis and added results using the Eppler 423 airfoil using Ansys Fluent and XFLR5 software, highlighting the robustness of computational fluid dynamics compared to the panel method.

Still on the subject of plain flaps, Jawahar et al. (2018) backed up the DES-based CFD analysis of the NACA 0012 airfoil with wind tunnel experiments to test modifications to the trailing edge camber of these models. The airfoils were tested with morphing flaps having different camber profiles for the deflection angles of $\delta = 5°$ and $\delta = 10°$, examined over a wide range of angles of attack and Reynolds numbers (around 10^5) using both methodologies. While the experimental results showed high levels of drag for low angles of attack, the CFD analysis served to attribute this behavior to recirculation and increased unsteady flow observed in the modified airfoils that were not present in the unmodified airfoil. The study concluded that even a small change in the airfoil trailing edge camber (independent of the flap position) is capable of generating better aerodynamic performance of the surface.

When it comes to other types of flap, Iqbal et al. (2019) studied the efficiency of the Gurney flap to improve aerodynamic efficiency while trying to minimize the generated drag. To do this, the author introduced porosity (punctures) in the structure to minimize the total pressure loss and used Ansys Fluent software to simulate the flow with a Reynolds number of $Re = 2.1 \cdot 10^6$. Various levels of porosity were analyzed with flaps of different dimensions and the one with 20% porosity and a length corresponding to 3% of the chord proved to be the most efficient. Meanwhile, the work by Tan (2020) numerically analyzed the flow over a wind turbine airfoil (S809) by adding both flap configurations (plain and Gurney). The simulations were carried out at a Reynolds number $Re = 10^6$, over a range of angles of attack and using different turbulence models — namely the Spalart-Allmaras (SA), SST k-ω and Wray-Agarwal (WA) — which showed similar results.

Using another flap configuration, the work by Murayama and Yamamoto (2004) studied the Fowler flap in 2D and 3D numerical simulations using the NLR-7301 airfoil using a custom solver. For the two-dimensional simulations, various angles of attack were analyzed for a Reynolds number $Re = 3.51 \cdot 10^6$, while the three-dimensional wing-fuselage configuration simulations were performed at $Re = 15 \cdot 10^6$. The author's main objective was to investigate the effect of the distance from the boundaries of the computational domain and the type of mesh used (structured and unstructured). Results showed that a certain density of elements in the far-field is necessary for correct drag prediction, and that both structured and unstructured meshes presented results that matched experimental data.

Similarly, Silva Oliveira (2017) described a low Reynolds number Fowler flap design aimed at small-scale aircraft development. Using OpenFOAM, the author modified various geometric characteristics of the flap (flap chord, angle, gap and overlap) in order to choose the combination with the best dynamic performance. Numerical simulations were carried out using the SST k-ω turbulence model and a Reynolds number of $Re = 2 \cdot 10^5$. The flap configuration with the most satisfactory results had 25% chord flap with a 2.5% gap, 2% overlap and 30° flap deflection.

The Fowler flap is constantly paired with another type of high-lift device, the slat, to form what is called a three-element high-lift configuration (slat, main wing, and flap). Works such as that by Sarjito et al. (2017), which analyzed this configuration coupled to the NACA 2410 airfoil using Ansys. The airfoil's geometric parameters and different angles of attack were studied. Murayama et al. (2006) did a more complete analysis, again evaluating the effect of different turbulence models on the simulation results of a three element high-lift airfoil. Aerodynamic force results were similar regardless of the turbulence model used for low angles of attack, but for steeper angles the SST k-ω model gave better results near the stall angle.

2 HIGH-LIFT DEVICES

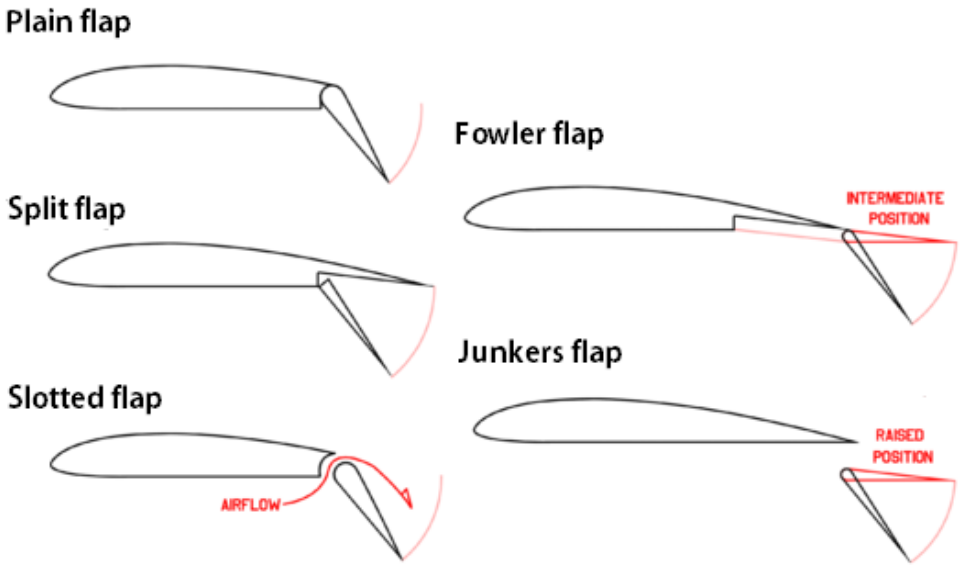
High-lift devices are essential equipment in reducing take-off and landing distances for aircraft, found on most modern aviation aircraft, developed for use in different flight stages and making it possible to operate an aircraft in different airspeeds. The diversity of configurations of these surfaces in the aviation industry reflects their evolution over time, designed at various historical moments in the industry, to solve distinct problems and using several methods and technologies to fulfill their objective, to increase the lift force, which is defined by the Equation (1).

$$L = \frac{1}{2} \cdot \rho V^2 \cdot S \cdot C_L \tag{1}$$

where ρ represents the air density, V is its relative velocity in relation to the wing, S is the reference area and C_L is the coefficient of lift, which is intrinsic to each geometry and depends on the camber of the airfoil, the chord of the profile and the angle of attack.

Whether by increasing the effective wing area, the effective camber angle or even more complex boundary layer control, most of these devices are capable of generating high-lift even for low angles of incidence. Trailing edge devices greatly influence the distribution of lift over the wing and have a profound effect on the structural design, in this work a few commonly found configurations will be discussed, which are presented in Figure 1.

Figure 1 – Different high-lift configurations



2.1 PLAIN FLAP

The plain flap is the simplest of the geometries and was the first to be developed and tested. It is obtained by deflecting a portion of the trailing edge of the airfoil, as can be seen in Figure 1, the main effect of this rotation is to increase the effective camber. Geometric characteristics of this type of configuration are the deflection angle (normally 15°), hinge location and the flap chord (maximum 30% of the airfoil chord).

Experimental results of Monte et al. (2012) highlight a reduction in the stall angle of the aerodynamic profile, since it anticipates the separation of the flow due to energy loss, while maintaining its slope, the drag generated is greater compared to the clean airfoil. It was popular when it was introduced because it allowed a greater angle of descent at the same airspeed. Nowadays this type of flap is used where simplicity and manufacturability are the most important factors, such as in light aircrafts, for example the Diamond DA42 Twin Star in Figure 2.

Figure 2 – Diamond DA42 Twin Star as an example of an aircraft with plain flaps.



Source: Jet Photos.

2.2 SPLIT FLAP

Another example of a simple configuration with low aerodynamic efficiency, the split flap is similar to its forerunner, deflecting only a portion of the trailing edge around a point while the rest remains fixed, as shown in Figure 1. Developed by Orville Wright and James M. H. Jacobs in 1924 (GUDMUNDSSON, 2022), one of the advantages of using split flaps is that the effects of separation on the airfoil's upper surface are less damaging, since the airfoil's suction region remains unchanged. For this reason, the split flap has a lift coefficient curve with larger stall angles, generally presenting similar slopes.

When fully deflected (from 60° to 70°) this type of flap can be used as a spoiler, a component that purposely increases the drag generated for the descent and landing phases and can actually perform better. Since it can heavily increase drag without decreasing lift,

it makes the approach to landing easier to controll. The increase in maximun lift is a little lower when compared to more sophisticated flaps types, not being used in mored airlines. The split flap can be found on old aircrafts such as the Supermarine Spitfire in Figure 3.

Figure 3 – Supermarine Spitfire as an example of an aircraft with split flaps.



Source: Jet Photos.

2.3 SLOTTED FLAP

Represented in Figure 1, this type of flap has a gap between the main element and the moving part, the deflection motion combines rotation and translation and increases the airfoil chord length by 5% to 10% . This configuration and its variations are among the most widely used nowadays due to their efficiency and they can be found on various types of aircraft, both small and large; the Cessna 172 Skyhawk in Figure 4 is an example. This type of flap has a typical chord of 25% to 30% of the airfoil length, and the gap between the elements is adjustable to manipulate the airflow and increase lift. Its idea was introduced in the 1920s through research by the British manufacturer Handley-Page.

Figure 4 – Cessna 172 Skyhawk as an example of an aircraft with slotted flaps.



Source: Chris Rose.

With such gaps, the high-pressure airflow is suctioned to the lower pressure region (upper surface), re-energizing the boundary layer and preventing it from separating from the airfoil surface. As a result, the stall occurs at higher angles of attack, generating more lift than the other configurations presented, and less drag is generated due to the lower wake generated downstream. There are numerous variations of the slotted flap, including the double slotted flap, where the second element is divided into two parts, and a type of flap discussed further on, the Fowler flap.

2.4 FOWLER FLAP

Considered a further development of the slotted flap, this type of configuration moves backwards before fully deflecting, as shown in Figure 1, increasing the effective area, chord and camber of the airfoil as well as having the advantages of the slot effect, as opposed to another similar configuration, the Gouge flap. Most slotted flaps are not considered Fowler flaps since the most notable feature of Fowler flaps is the large increase in chord it provides, since the lift coefficient takes into account the original chord of the airfoil, its value is overestimated. It was developed by Harlan D. Fowler in 1924 and first commercialized on the "Lockheed L-10 Electra" in 1935. Since then, it has become popular and received further upgrades, such as the Double-Slotted Fowler Flap, which increases the benefits of high-pressure air suction from the inner surface.

This kind of flap is one of the most widely used in today's industry, because it offers high levels of lift at low angles of attack and low speeds, and because it delays the separation of the boundary layer and consequently the stall. With so many advantages, their design is more meticulous and small variations in geometric characteristics strongly impact their performance, Silva Oliveira (2017) shows this process in more detail. Fowler flaps are often used on large jets where their increased wing area helps generate lift for takeoff, as for example on the Boeing 747 in Figure 5.

Figure 5 – Boeing 747 as an example of an aircraft with fowler flaps.



Source: Jet Photos.

2.5 JUNKERS FLAP

The Junkers flap (also called an external flap) is an unusual high-lift device, in that it is located entirely outside the wing, as shown in Figure 1. Like the Fowler flap, this configuration also increases the effective area along with the effective camber of the airfoil when deflected. Due to the gap between the main element and the flap, this type of configuration can also benefit from the slot effect that other flap types have, such as delayed boundary layer detachment. The external flap is most notable for its use on the German Junkers 52-3 military (and commercial) transport aircraft, designed around 1930, as shown in Figure 6. One of its main advantages is that it adds virtually no drag to the to the installation and can even reduce it by some if it is correctly located close to the trailing edge.

This type of flap is not widespread today because, at high deflection angles, the flap does not generate a large enough Cl_{max} on its own, requiring other devices to improve its viability. However, it allows for a simple installation that can be the right choice for selected applications, since the flap resides outside the boundary layer, making it more effective at low deflection angles.

Figure 6 – Junkers 52 as an example of an aircraft with junkers flaps.



Source: Jet Photos.

3 COMPUTATIONAL FLUID DYNAMICS (CFD)

Computational fluid dynamics (CFD) is the science of using computers to predict liquid and gas flows based on the governing equations of conservation of mass, momentum, and energy. CFD is used wherever there is a need to predict fluid flow and heat transfer, or to understand the effects of fluid flow on a product or system. CFD analyzes different properties of fluid flow, such as temperature, pressure, velocity, and density, and can be applied to a broad range of engineering problems across industries. It solves equations through a numercial model, that must contain some critical elements that affect the accuracy of its results, depending on the methods and models used. According to Ferziger and Peric (2002), the main components of a numerical model are:

Mathematical model

It involves the governing equations of the problem (such as the Navier-Stokes equations), models used to simplify the behavior of certain properties (such as the different turbulence models) and assumptions made (such as the hypothesis that the flow is incompressible and isothermal). The accuracy of the results is a product of the mathematical model used; if it is not adequate, the simulation will not well represent the physical behavior. The choice of a good mathematical model is the result of a trade-off between accuracy and computational cost. In Chapter 4, the specifics of this topic are better covered.

Discretization model

The discretization model is the method used to apply the continuous differential equations to a discrete mean in time and space. Different methods are used by the various software programs on the market, including the finite difference method, the finite volume method and the finite element method. This work will use the finite volume method, where the computational domain is divided into a finite number of control volumes and the equations are integrated over the volume.

Mesh

The mesh is the computational domain where the discretization model and boundary conditions are applied. The mesh can be structured or unstructured, in which the location of the elements follows a pattern and they have the same number of neighboring cells, but it is more difficult to implement in complex geometries, while an unstructured mesh (which does not follow this pattern) produces less accurate results if it has elements with high orthogonality. In Chapter 5 the mesh used is generated and discussed.

Solution and approximation methods

To numerically solve the differential and integral equations produced by the previous methods, different numerical approximation methods can be used. The chosen numerical schemes influence the accuracy of the model, the speed of the calculation and the memory required to solve the system. Among the implicit, segregated and coupled methods, different strategies are used to achieve a numerical result efficiently and accurately. More details on the available solution methods are discussed in Chapter 4.

In addition, methods for interpolating the calculated quantities must also be chosen, two of which are commonly adopted in CFD, the centered difference method and the Upwind method. The Upwind method will be used in this work and interpolates the values of different quantities based on the velocity vector and, in general, reduces the interpolation error.

Convergence Criteria

As it is not an exact method, there must be a criterion to define that the simulation has reached an acceptable result. To do this, it is possible to evaluate the variation of the properties of interest (such as total heat exchange or lift coefficient) or the maximum normalized residual. In this way, when the residuals of all the equations or the variation of the properties of interest in a given iteration fall below the established threshold, the system is considered to have converged.

3.1 OPENFOAM®

OpenFOAM® (Open Field Operation And Manipulation) is a free open source software, i.e. whose source code is made public by its developers for free use and modification. The software was initially developed by the company OpenCFD Ltd and officially launched in 2004, based on the post-processing tool FOAM, created in 1989 by Henry Weller. Using a C++ based, object-oriented programming language, the software is used to develop solvers and other utilities for solving problems based on systems of equations, but mainly those in computational fluid dynamics (OPENCFD LTD., 2017).

The software is widely used for academic and commercial purposes in various areas of science and engineering, including tools for solving complex problems involving chemical reactions, turbulence, heat transfer, acoustics, solid mechanics and electromagnetics. Its source code is under constant development and improvement, OpenFOAM® is professionally released every six months to include customer sponsored developments and contributions from the community and quality assurance is based on rigorous testing, according to the OpenFOAM: User Guide v2112 (2017). Furthermore, the freedom and ease of access means that it is often used in academia for research and technology development purposes.

Upon installing OpenFOAM®, the basic software structure contains the following main directories, among others:

- *applications*: Solvers and utility tools.
- *doc*: The software documentation.
- *src*: The OpenFOAM® core libraries.
- *tutorials*: A list of test cases that address the various functionalities included in the software.

When analyzing a case, depending on the solver used, different files will be needed, however, in every simulation carried out in OpenFOAM®, at least three directories with their respective files must exist:

- *0*: It represents the initial condition or first iteration of the problem. It contains a file for each scalar or vector field analyzed (pressure, velocity, temperature, etc.). In this folder you can determine boundary conditions and initialize variables.
- *constant*: It holds the properties of the simulation that do not change with each iteration, such as constant material properties (viscosity, specific heat, etc.). In addition, the mesh used is saved in this directory.
- *system*: This folder contains the files that will govern the simulation. This folder also contains the post-processing and mesh generation/manipulation functions. Within this directory, some files are mandatory:
    - *controlDict*: Main file that defines the simulation controls. Start and end time, time interval between each simulation, format of each result, among other commands. Functions can also be declared in this file.
    - *fvSchemes*: This file defines the numerical schemes to be used for each operation (divergent, derivatives, etc.).
    - *fvSolution*: It sets the convergence parameters, solvers of the linear systems and relaxation factors.

4 NUMERICAL METHODOLOGY

4.1 SOLVERS

OpenFOAM® allows the use of different solvers based on the finite volume method to solve problems. They differ in the governing equations used and are recommended depending on the case studied. For incompressible fluid flow, some of the available solvers are listed:

- boundaryFoam: Solver for turbulent, permanent and one-dimensional flow. Used as a tool for generating boundary conditions for other simulations.
- icoFoam: Solver for laminar and transient flow of Newtonian fluids.
- nonNewtonianicoFoam: Laminar and transient flow solver for non-Newtonian fluids.
- simpleFoam: Solver for turbulent and permanent flow.
- turbFoam: Solver for turbulent and transient flow.

For this case study, the most suitable solver is simpleFoam.

4.1.1 simpleFoam

Developed for simulating incompressible flows in the steady state, simpleFoam allows the use of different turbulence models. It handles laminar and turbulent, single-phase and subsonic flows under isothermal conditions, accommodating both Newtonian and non-Newtonian fluids. The solver uses the SIMPLE method (Semi-Implicit Method for Pressure Linked Equations) to solve the linear continuity and momentum conservation equations (presented in Equations (2) and (3)) through the coupling of velocity and pressure, augmented by under-relaxation techniques to enhance convergence.

$$\frac{\partial \rho}{\partial t} + \nabla \cdot (\rho \mathbf{u}) = 0 \tag{2}$$

$$\frac{\partial}{\partial t}(\rho \mathbf{u}) + \nabla \cdot (\rho \mathbf{u}\mathbf{u}) = -\nabla p + \nabla \left((\mu + \mu_T) \left(\nabla \mathbf{u} + \nabla (\mathbf{u})^T \right) \right) + \mathbf{f_B} \tag{3}$$

where ρ represents the fluid density, derived as a function of time t, $\mathbf{u}$ is the velocity vector, denoted in bold, p is the pressure field, μ is the fluid viscosity and $\mathbf{f_B}$ represents the linear momentum source term vector.

The equations have high non-linearity, and Equation (3) is a vector equation with its components, but the main problem that cannot be solved directly is the lack of an explicit equation to compute the pressure field present in the linear momentum conservation equation. While the velocity can be evaluated through the conservation of linear momentum, the pressure field cannot be computed through the continuity equation, this coupling can be made explicit by writing the equations in the following form:

$$\mathbf{Av} = \begin{pmatrix} \mathbf{F} & \mathbf{B}^T \\ \mathbf{B} & \mathbf{0} \end{pmatrix} \begin{pmatrix} \mathbf{u} \\ \mathbf{p} \end{pmatrix} = \begin{pmatrix} \mathbf{f_B} \\ \mathbf{0} \end{pmatrix} \tag{4}$$

where the matrix $\mathbf{A}$ contains the coefficient matrices $\mathbf{F}$ and $\mathbf{B}$.

The presence of a null diagonal block in the system indicates a saddle point problem and that an equation for the pressure is required to solve the (MOUKALLED et al., 2016) problem. It is possible to decompose the $\mathbf{A}$ matrix into an upper triangular matrix ($\mathbf{U}$) and a lower triangular matrix ($\mathbf{L}$), as shown:

$$\mathbf{A} = \begin{pmatrix} \mathbf{F} & \mathbf{B}^T \\ \mathbf{B} & \mathbf{0} \end{pmatrix} = \begin{pmatrix} \mathbf{F} & 0 \\ \mathbf{B} & -\mathbf{B}\mathbf{F}^{-1}\mathbf{B}^T \end{pmatrix} \begin{pmatrix} \mathbf{Id} & \mathbf{F}^{-1}\mathbf{B}^T \\ \mathbf{0} & \mathbf{Id} \end{pmatrix} = \mathbf{LU} \tag{5}$$

where $\mathbf{Id}$ represents an identity matrix.

The SIMPLE method then follows a segregated solution strategy, following an iterative procedure where the momentum equation is solved using the pressure field, which is the result of the previous iteration. The resulting velocity field, which does not necessarily respect the continuity equation, is applied to the pressure equation whose solution is used to correct the fields obtained in order to comply with mass conservation. A new iteration then takes place using the corrected values. The algorithm is described in Equations (6) and (7)

$$\begin{pmatrix} \mathbf{Id} & \mathbf{D}^{-1}\mathbf{B}^T \\ \mathbf{0} & \mathbf{Id} \end{pmatrix} \begin{pmatrix} \mathbf{u} \\ \mathbf{p} \end{pmatrix} = \begin{pmatrix} \mathbf{u}^* \\ \mathbf{p}^* \end{pmatrix} \tag{6}$$

$$\begin{pmatrix} \mathbf{F} & 0 \\ \mathbf{B} & -\mathbf{B}\mathbf{D}^{-1}\mathbf{B}^T \end{pmatrix} \begin{pmatrix} \mathbf{u}^* \\ \mathbf{p}^* \end{pmatrix} = \begin{pmatrix} \mathbf{f_B} \\ \mathbf{0} \end{pmatrix} \tag{7}$$

where the matrix $\mathbf{F}^{-1}$ has been approximated to the inverse of its diagonal, denoted $\mathbf{D}^{-1}$, and $\mathbf{u}^*$ and $\mathbf{p}^*$ represent the intermediate values of the velocity and pressure fields.

Equation (3) can be simplified and discretized, so that the convective and diffusive terms of the equation depend on linear coefficients (a^u) and on the velocity evaluated in the generic cell of interest (with subindex C) and in its neighboring cells (with subindex N). The discretization is shown in Equation (8).

$$a_C^u u_C + \sum_{NB\ C} a_N^u u_N = f_B - \nabla p \tag{8}$$

OpenFOAM® defines the $H(u)$ operator as:

$$H(u) = f_B - \sum_{NB\ C} a_N^u u_N \tag{9}$$

logo:

$$u_C = \frac{H(u)}{a_C^u} - \frac{\nabla p}{a_C^u} \tag{10}$$

by applying Equation (2):

$$\nabla \cdot \left(\frac{H(u)}{a_C^u} \right) = \nabla \cdot \left(\frac{\nabla p}{a_C^u} \right) \tag{11}$$

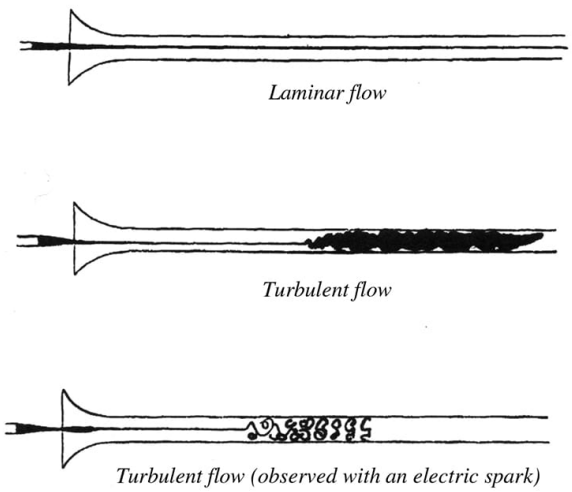
Thus, the solver follows the algorithm presented above, applying the discretization for each element of the domain and for each component of the velocity field.

1. Solve Equation (8).
2. Solve Equation (11) for p.
3. Solve Equation (10) for u_C.
4. update u_C and p.

4.2 TURBULENCE MODEL

A given flow can generally be classified as laminar or turbulent. Laminar flow is smooth and, as the name suggests, flows in layers, while turbulent flow is chaotic and has a high degree of mixing between different layers of fluid, with the presence of vortices and instabilities. Reynolds (1883) notably carried out experiments involving the flow of water and dye in a tube and observed this behavior, as can be seen in Figure 7. In addition to presenting the formulation of a dimensionless number that quantified turbulent behaviour based on fluid and flow properties, characterized as a ratio between the inertial forces and the viscous forces of the flow, the widely used Reynolds number (Re).

Figure 7 – Experimental visualization conducted by Osborne Reynolds



Source: Reynolds (1883).

$$Re = \frac{\rho \cdot U \cdot L}{\mu}$$

where μ is the viscosity of the fluid, U represents a characteristic velocity of the flow and L a characteristic length, somewhat arbitrarily, these properties vary depending on the situation analyzed.

For numerical simulation purposes, laminar flow has a much lower computational cost than turbulent flow. High Reynolds number flows are unsteady, enormously irregular in space and time, three-dimensional, rotational, dissipative (in terms of energy), and diffusive (transport phenomenon), creating a much more complex problem when using a method that simply solves the Navier-Stokes Equations, called Direct Numerical Solution (DNS). Therefore, when analyzing turbulent flows, it is common to use turbulence models. Turbulence models are generally classified according to the governing equations and the numerical methods for calculating turbulent viscosity (a property that simulates the effects of turbulence):

- DNS (Direct Numerical Solution): Already mentioned above, it does not apply any turbulence model and calculates the velocity fluctuations point by point.
- LES (Large Eddy Simulation): Developed to model small-scale vortices, it uses a filtered value of the results of the Navier-Stokes equations. Its implementation is rare because it requires a lot of computing power.
- RAS (Reynolds Averaged Simulation): Uses average values and fluctuations in the fluid equations, the effect of turbulence is modeled in the fluctuations at each iteration. It is widely used because it requires a modest amount of hardware, computational time, and human effort.

For the case studied, the RAS turbulence model will be adopted, due to the computing power available.

4.2.1 Mesh requirements

For the turbulence model to be effective, different meshing requirements have to be met, especially in regions close to walls. To quantify the mesh refinement required, the variable y^+ represents a dimensionless height of the first mesh element near a wall, which can be interpreted as a local Reynolds number, as shown in Equation (12).

$$y^+ = \frac{\rho \cdot y \cdot u_\tau}{\mu} \tag{12}$$

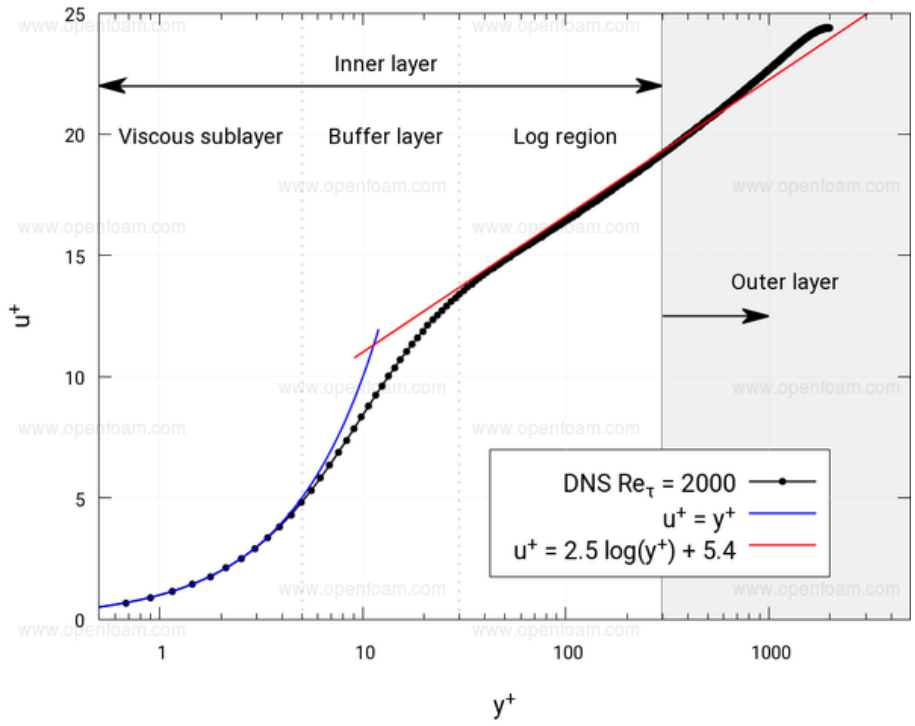
where y is the distance to the wall and u_τ represents the shear velocity, which in turn can be described in terms of the shear stress in the wall (τ_w), shown in Equation (13). Another important value is the dimensionless velocity U^+, defined as a function of the two velocities presented above, shown in Equation (14).

$$u_\tau = \sqrt{\frac{\tau_w}{\rho}} \tag{13}$$

$$U^+ = \frac{u}{u_\tau} \tag{14}$$

These parameters were related by von Karman (1931) in the boundary layer region in what is called the Law of the Wall and then analyzed by Moser et al. (1999), the results of which are shown in Figure 8. It can be seen that in the viscous sublayer, for a low local Reynolds number (y^+), the behavior of the dimensionless velocity is linear with the distance from the wall, while in the log region the flow is turbulent and the velocity follows an empirical logarithmic function.

Figure 8 – Mean velocity in function of wall distance



Source: Moser et al. (1999).

This analysis serves to point out that, for an intermediate local Reynolds number, the dimensionless velocity does not follow any of the approximations presented, and therefore it should be avoided that the height of the first mesh element results in a value of y^+ between 5 and 30. For mesh generation, this point should be observed. When the model has no wall function, which dictates the behavior of the properties in these regions, it is recommended that the first element be in the region where $y^+ < 5$.

4.2.2 RAS

There are several turbulence models that are classified as RAS models, which vary in terms of the number of equations used, the level of complexity, stability and with

different limitations and advantages, some of them are:

- Spalart-Allmaras: 1-equation model, does not use wall functions and is widely used in transonic aerodynamic flows, but is not recommended for stall flows.
- k-epsilon: 2-equation model, solves for turbulent kinetic energy (k) and turbulent dissipation (ϵ) using wall functions, recommended for flow around complex geometries, but does not cope well with adverse pressure gradients.
- k-omega: Similar to k-epsilon, it uses ω as the specific rate of turbulent dissipation, improving accuracy in internal flows. However, it is not very stable and is sensitive to initial conditions.
- k-omega SST: Combination of the k-epsilon and k-omega models in their optimal configurations, convenient when there is flow separation, but equally unstable.

The Spalart-Allmaras model was designed specifically for aerospace applications and aerodynamic flows involving wall-bounded flows and has been shown to give good results for boundary layers subjected to adverse pressure gradients. It is known for being a one equation model based on a modified turbulence viscosity ($\tilde{\nu}$), which is easier to solve numerically than ν_t, as the solution is likely to be close to linear. The Equation (15) represents the equilibrium of this variable in the control volume, and the the turbulence viscosity is obtained using:

$$\mu_t = \rho \cdot \tilde{\nu} \cdot \frac{\chi^3}{\chi^3 + c_{v1}^3}$$

where

$$\chi = \frac{\tilde{\nu}}{\nu}.$$

$$\frac{\partial \tilde{\nu}}{\partial t} + \nabla \cdot (\mathbf{u} \cdot \tilde{\nu}) = \frac{c_{b1}}{2} \cdot \left(\nabla \mathbf{u} + \nabla(\mathbf{u})^T\right) \cdot \tilde{\nu} + \frac{1}{\sigma} \cdot \left(\nabla(\nu + \tilde{\nu}) \nabla \tilde{\nu} + c_{b2} \nabla \tilde{\nu}^2\right) - c_{w1} f_w \left(\frac{\tilde{\nu}}{d}\right)^2 \quad (15)$$

where c_{b1}, c_{b2}, c_{w1}, c_{v1}, f_w and σ are experimentally defined turbulence model coefficients.

For this reason, the Spalart-Allmaras model was selected to solve the equations of the problems presented in this work. By choosing a single turbulence model, the processes of mesh generation and allocation of boundary conditions are simplified. As for the mesh, this model requires the viscosity-affected region of the boundary layer to be properly resolved ($y^+ \simeq 1$).

5 PREPROCESSING

5.1 MESH GENERATION

The mesh generation begins with the definition of the computational domain. Based on the work of authors like Kumar and Kumar (2013), Ladson (1988), Santos Nogueira (2023), Şahin and Acir (2015) and Unde and Sutar (2018), a "two-dimensional" domain was adopted with a semicircle-shaped fluid inlet and a rectangular wake region, since OpenFOAM® only works with three-dimensional simulations, it is necessary to create a 3D domain and adjust the number of elements and boundary conditions so that only two dimensions are solved. The mesh extends vertically at a distance of 18 times the chord length in both directions, likewise upstream of the flow, while downstream, the mesh in the wake region is 30 airfoil chords long.

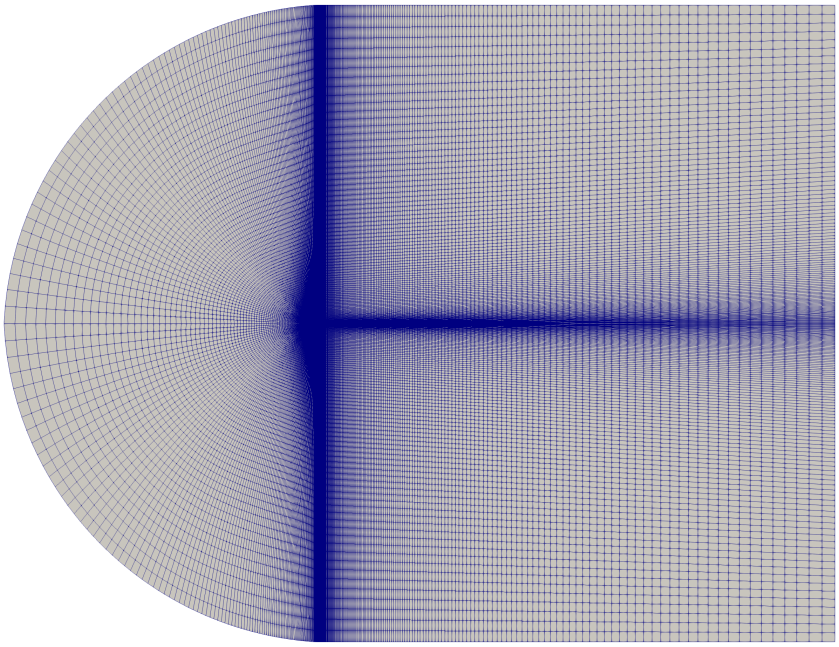
The meshes of all the cases analyzed in this work will be created following the same procedure, using the mesh generation tools *snappyHexMesh* and *blockMesh* from OpenFOAM®. *snappyHexMesh* is a utility that generates three-dimensional meshes with hex and split-hex elements around triangulated surface geometries in Stereolithography (STL) format. The mesh approximates the geometry provided through refinement iterations of a background mesh, as well as having other mesh controls such as refinement levels and adding layers of elements. It is useful for creating external flow meshes, as it conforms to complex geometries with a certain level of precision and is easily applicable to airfoils of different geometries (such as with the addition of different flap configurations). Solid Edge software is used to create the geometry, a .dat file containing the two-dimensional coordinates of the airfoil being analyzed is responsible for creating the curves which are then edited and extruded, and then converted into an .STL file.

5.1.1 *blockMesh*

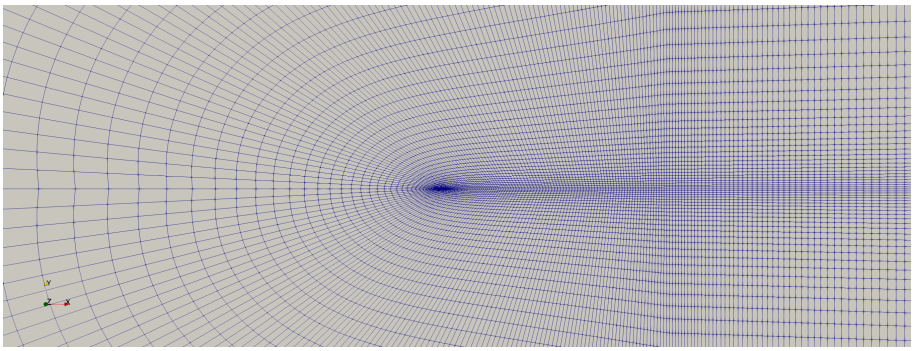
To create the background mesh, *blockMesh* is used, the most basic mesh creation tool inherent to OpenFOAM®, which breaks down the domain into one or more three dimensional, hexahedral blocks. The *blockMeshDict* file located in the system folder contains all the mesh creation settings and preferences, whose contents will be briefly discussed in this section.

The result of the initial mesh is shown in Figure 9. It is worth noting that some refinement settings are already defined in the background mesh, near the origin of the system (location of the airfoil) and in the wake region. It is important to note that the central region must be contained within the surface that delimits the airfoil so that there are no elements with high skewness.

Figure 9 – Background mesh generated by *blockMesh*, showing (a) whole computational domain and (b) zoomed origin region.



(a)



(b)

5.1.2 *snappyHexMesh*

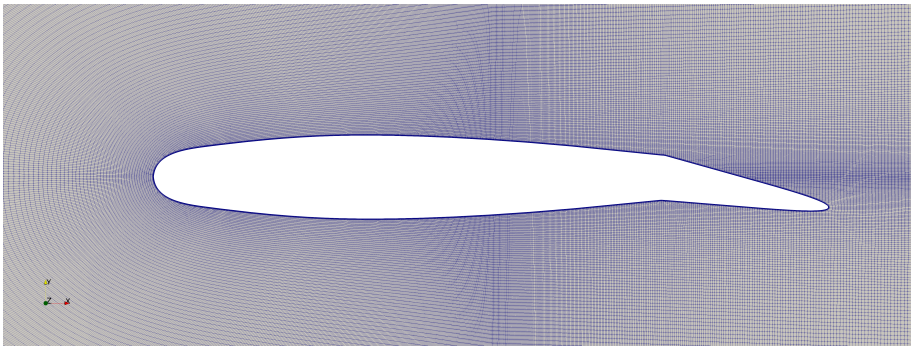
Once the background mesh has been created, the *snappyHexMesh* commands can be configured in the *snappyHexMeshDict* directory. All the geometries used to modify the initial mesh are declared in the *geometry* subdirectory. In this case, only the airfoil .STL file will be declared, at which point the file must be stored in a folder named *triSurface* inside the *constant* folder.

The generation of the elements close to the surface is controlled by the *addLayersControls* subdirectory. In the case of the meshes used in this work, it was chosen to create a boundary layer whose thickness is 9 elements, with an expansion rate equal to 2 and so that the thickness of the last element is equal to 1 mm. In addition, a refinement region is inserted during the generation of the castellated mesh, all elements at a distance

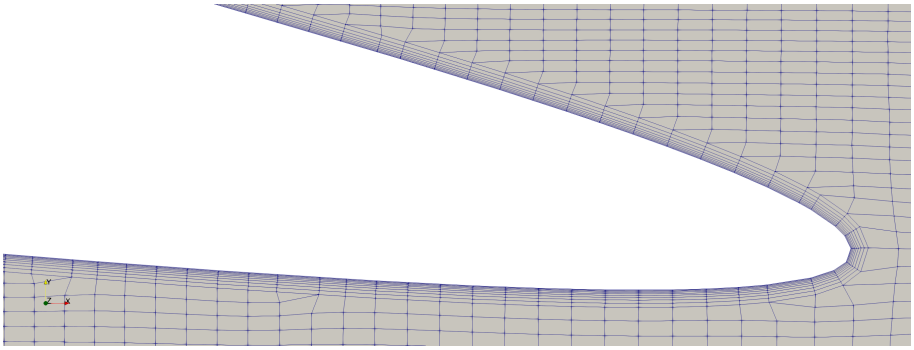
of 2.5 m or less are refined to the next level.

The result of the final mesh is shown in Figure 10 for an airfoil with a generic flap. Note that the refinement region starts in an area away from the walls, to ensure that the difference in cell dimensions does not affect the results, and the transition layers on the airfoil wall can be seen. *snappyHexMesh* automatically modifies the mesh saved in the *constant* folder, and configures the new region created with the name airfoil, and sets its type to wall.

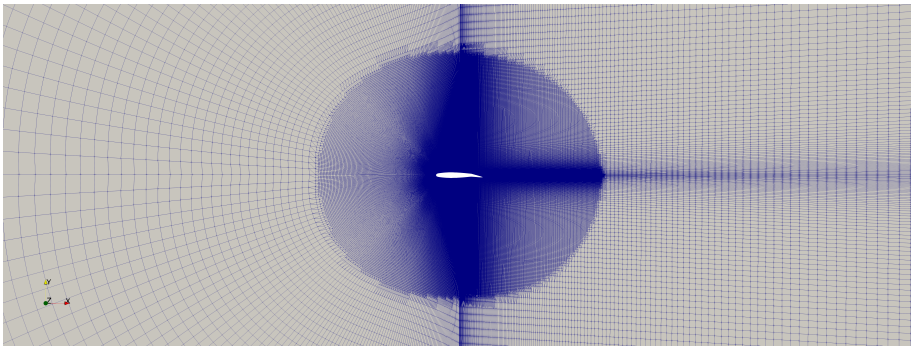
Figure 10 – Mesh generated by *snappyHexMesh*, showing (a) the refinement region near the airfoil, (b) zoomed transiotion layers and (c) farfield region.



(a)



(b)



(c)

5.2 BOUNDARY CONDITIONS

The boundary conditions for each simulation are defined in the *0* folder and must be declared for each patch and variable in the problem. The conditions used in this work are shown in Table 1.

Table 1 – Compiled boundary conditions for the problem variables.

Patch	**Condition**	**Value**
	Velocity (U)	
Inlet	freestreamVelocity	$U_\alpha\ m/s$
Outlet	freestreamVelocity	$U_\alpha\ m/s$
Front and Back	empty	-
Airfoil	fixedValue	$\mathbf{0}\ m/s$
	Kinematic pressure (p)	
Inlet	freestreamPressure	$0\ m^2/s^2$
Outlet	freestreamPressure	$0\ m^2/s^2$
Front and Back	empty	-
Airfoil	zeroGradient	-
	Turbulent kinematic viscosity (nut)	
Inlet	freestream	$v_{fluid}\ m^2/s$
Outlet	freestream	$v_{fluid}\ m^2/s$
Front and Back	empty	-
Airfoil	fixedValue	$0\ m^2/s$
	Modified kinematic viscosity (nuTilda)	
Inlet	freestream	$4 \cdot v_{fluid}\ m^2/s$
Outlet	freestream	$4 \cdot v_{fluid}\ m^2/s$
Front and Back	empty	-
Airfoil	fixedValue	$0\ m^2/s$

It should be noted that the boundary conditions at the inlet and outlet are set as freestream, which is a generic boundary condition that provides a free-stream condition whereby the mode of operation switches between fixed value and zero gradient based on the sign of the flow, if the flow enters the surface it is allocated as fixed value, and if it exits the zeroGradient condition is applied, for all variables. The value denoted U_α corresponds to the initial velocity vector which depends on the angle of attack chosen. For the airfoil wall, the no-slip condition is translated into the fixed velocity value condition with the null vector. For the turbulent viscosity, the fixed value of the input is approximated to the fluid viscosity, while for the Spalart-Allmaras model modified viscosity Rumsey (2024) recommends a value between 3 and 5 times the magnitude of ν_t. For the airfoil walls, the turbulent viscosity of the fluid is zero.

6 POSTPROCESSING

There are two ways of performing post-processing in OpenFOAM®, either by using a specific command in the command window in a simulation folder, along with the appropriate settings, or by including the function in the control directory of the case studied. In the latter case, the function can be executed at a predetermined interval and allows the user to track the evolution of the studied parameters via the *postProcessing* folder or the simulation time files. In addition to the native OpenFOAM® functions, this work used Matlab® software for processing and ParaView® for visual representation of the simulation data. The post-processing tools used in this work are listed below.

yPlus

The yPlus function object computes the near wall y^+ for turbulence models. Calculated based on Equation (12), the function returns the value of this variable for each selected time file.

residuals

The function computes the residuals of the chosen fields or variables at each calculated time interval. For the simulations carried out in this work, the pressure, velocity and modified turbulent viscosity fields were probed. To monitor the convergence of the simulation at each iteration, the *foamMonitor* function was used.

forces and forceCoeffs

Both functions are used to calculate the aerodynamic resulting force on a given surface from the properties of the flow. The former is used to calculate the normal forces (due to pressure, denoted F_p) and tangential forces (due to viscous contribution, denoted F_v) at the surface, shown in Equations (16) and (17). The forces are then divided into their lift and drag components.

$$F_p = \sum_i \rho_i \cdot s_{f,i} \cdot (p_i - p_{ref}) \tag{16}$$

$$F_v = \sum_i s_{f,i} \cdot (\mu \cdot R_{dev}) \tag{17}$$

where the subindex i indicates each of the elements contained in the patch, $s_{f,i}$ is the face area vector, p_{ref} is the atmospheric pressure and R_dev the deviatoric stress tensor, which constitutes only the anisotropic part of the stress tensor, since it is the only one that can carry momentum, and is defined by:

$$R_{dev} = \overline{u' \times u'} - \frac{2}{3} k \cdot I$$

where u' is the fluctuation of the velocity vector, k represents turbulent kinetic energy and I is the turbulent intensity.

Meanwhile, the *forceCoeffs* function calculates the coefficients of aerodynamic forces and moments, based on Equations (18) and (19).

$$C_L = \frac{2 \cdot L}{\rho \cdot V^2 \cdot S} \tag{18}$$

$$C_D = \frac{2 \cdot D}{\rho \cdot V^2 \cdot S} \tag{19}$$

where V represents the freestream velocity of the flow, and S a reference area, in this case as the rope is unitary and the simulation is 2D, the area is also unitary. These values are used as input for the function.

surfaces

Finally, the function is used to sample some calculated field in a specific region. In this work, the function was used to obtain the pressure values around the airfoil wall to calculate the pressure coefficient C_p, defined by Equation (20). The function returns a file for each selected time interval and Matlab® was used to process and display the data.

$$C_p = \frac{2 \cdot (p - p_{ref})}{\rho \cdot V^2} \tag{20}$$

7 LITERATURE COMPARISON

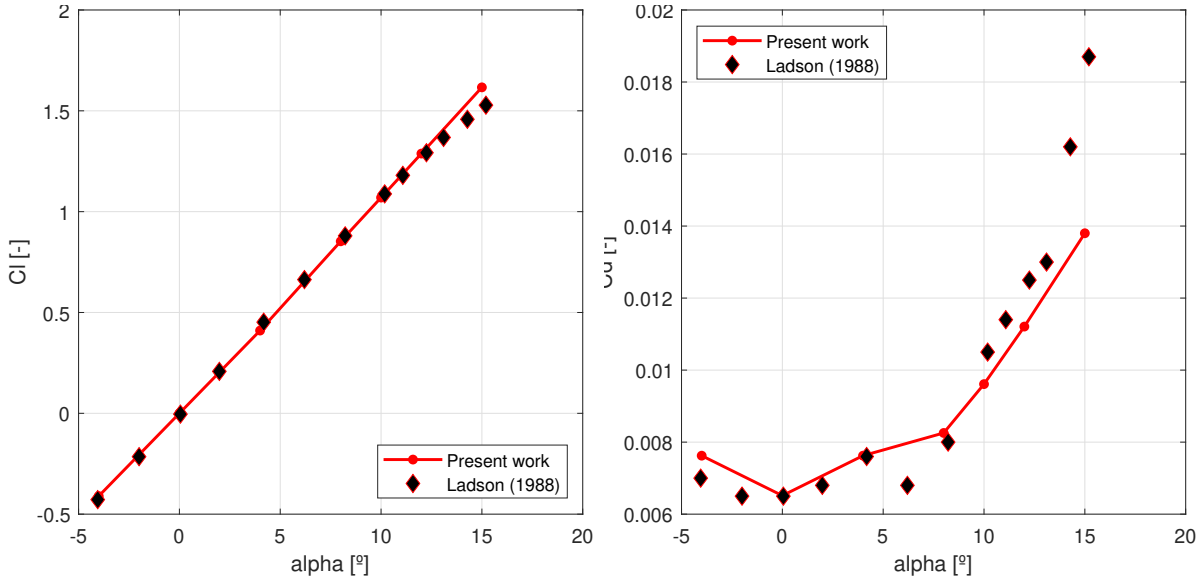
In order to assess the reliability of the numerical methodology used to generate the findings of this work, results obtained in the literature were compared using experimental and numerical data from other authors. Replicating the geometries and boundary conditions described by the authors, the OpenFOAM® software was used to carry out the numerical simulations of different airfoils.

7.1 LADSON (1988)

Ladson (1988) carried out a range of wind tunnel experiments using the NACA 0012 airfoil, varying the Reynolds number, Mach and angle of attack and analyzing the results of the aerodynamic coefficients. In order to replicate the same physical conditions as the experiment, a guide provided by OpenCFD Ltd. (2017) was used for the simulations. It was chosen to simulate a range of angles of attack between $-4°$ and $15°$ for a Reynolds number of $Re = 6 \cdot 10^6$. For this purpose, the velocity entering the domain was set at $U_\infty = 51.4815\ m/s$ and the turbulence model used was Spalart Almarras, specialized in aeronautical applications. Figure 11 contains a comparison of the drag and lift coefficient results obtained.

It is possible to see a match in the C_l and C_d data, even though the difference between the drag results is greater. According to Avraham (2024), the drag force is inherently more difficult to predict, compared to other phenomena, because it depends

Figure 11 – (a) Lift and (b) Drag coefficients results obtained in the present work and by Ladson (1988)



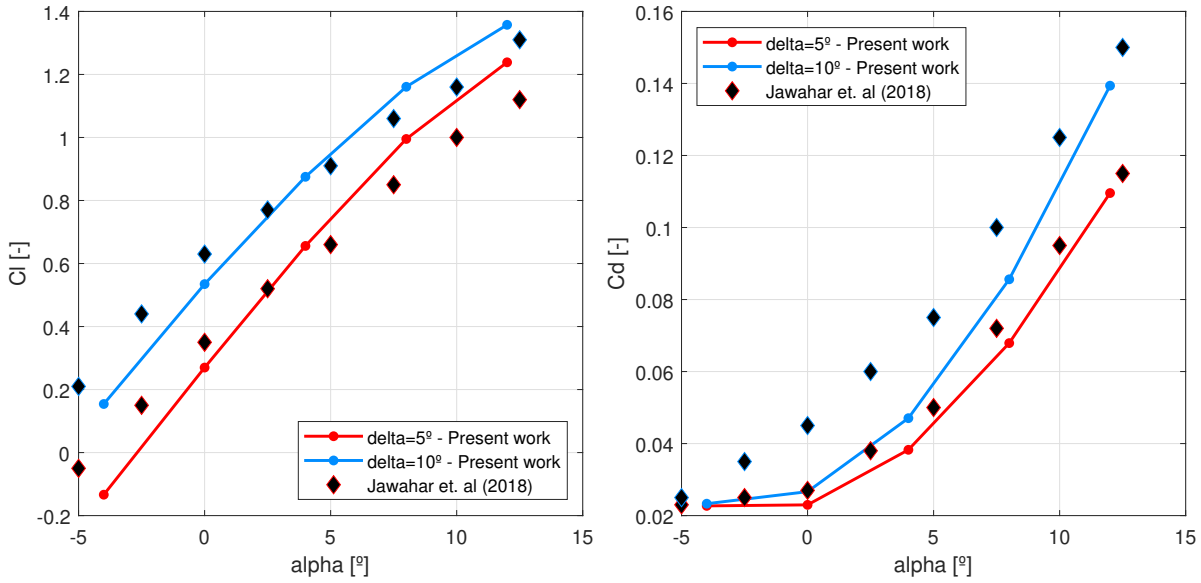
(a) (b)

Source: (LADSON, 1988).

on several factors that are calculated in a numerical simulation, imperfections in the turbulence model, mesh limitations and sensitivity to convergence affect this result more considerably.

7.2 JAWAHAR ET AL. (2018)

Figure 12 – (a) Lift and (b) Drag coefficients results obtained in the present work and by Jawahar et al. (2018)



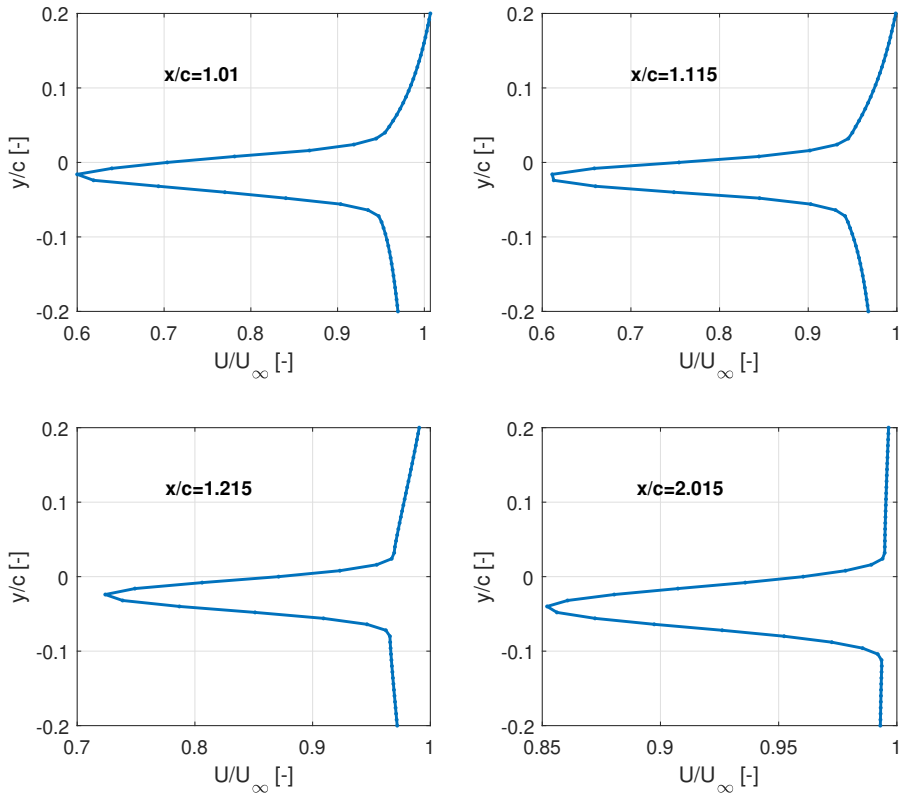
(a) (b)

Source: (JAWAHAR et al., 2018).

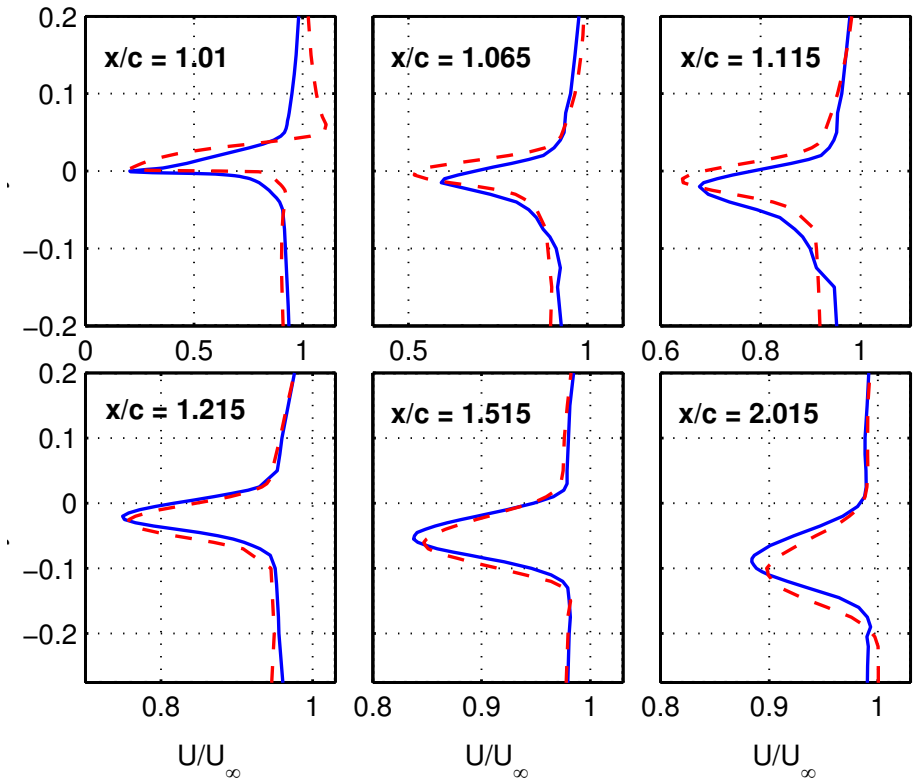
Jawahar et al. (2018) experimentally analyzed the performance of a NACA 0012 airfoil with flaps. Results of lift, drag and wake flow coefficients were obtained with different morphing flap camber profiles over a wide range of angles of attack and Reynolds numbers. The authors carried out experiments in a wind tunnel with flap airfoils deflected at 5° and 10° with an air inlet velocity $U_\infty = 25\ m/s$, corresponding to a Reynolds number $Re = 3.5 \cdot 10^5$. In an attempt to replicate the results of the experiments for the Hinged Flap, these same properties were adjusted in the OpenFOAM® software routine, using the same turbulence model and a kinematic viscosity $\nu = 7.1429 \cdot 10^{-5}\ m^2/s$. The results obtained in the simulation and those obtained by the author are shown in Figure 12. The behavior of the coefficients is similar to that discussed previously in the work by Ladson (1988), with the lift coefficient results showing greater accuracy than the drag results.

Figure 13 shows a wake flow-field comparison of both works, obtained by numerical simulation in OpenFOAM® using the velocity fields, and experimentally using hot-wire anemometry in the wind tunnel. For the sake of brevity, only a few dimensionless velocity profiles as a function of vertical position are shown for different horizontal chord distances for the airfoil with flap deflection for $\delta = 5°$ and angle of attack $\alpha = 0°$. It is possible to

Figure 13 – Wake velocity profiles at obtained (a) in the present work and (b) by Jawahar et al. (2018) for $\delta = 5°$ e $\alpha = 0°$.



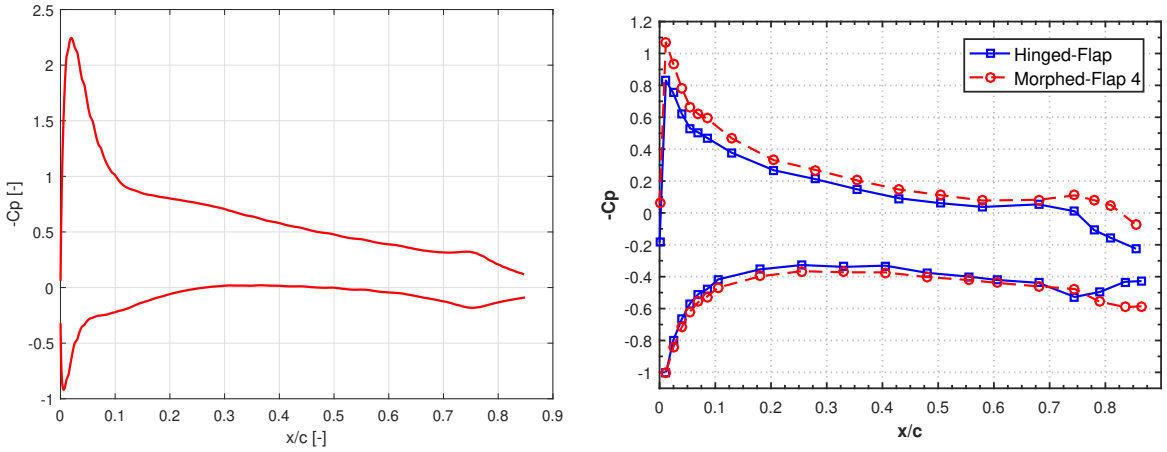
(a)



(b)

Source: (JAWAHAR et al., 2018).

Figure 14 – Pressure coefficient distribution over the flapped airfoil obtained (a) in the present work and (b) by Jawahar et al. (2018) for $\delta = 10°$ e $\alpha = 4°$.



(a) (b)

Source: (JAWAHAR et al., 2018).

observe the same behavior of translation of the peak velocity and decrease of the amplitude when increasing the distance from the chord.

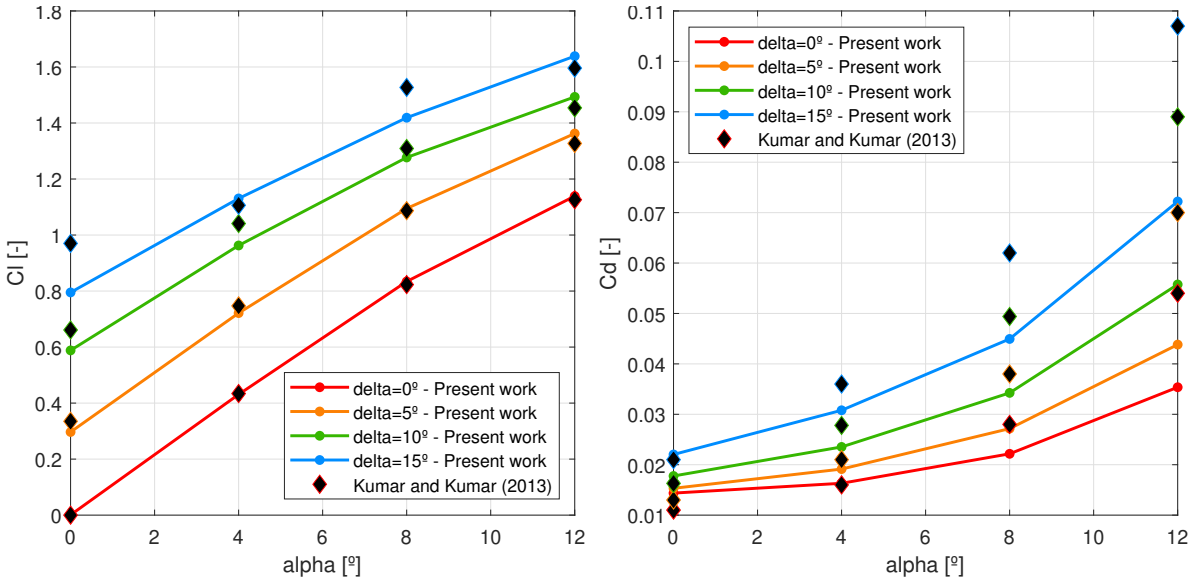
Finally, the results of the pressure coefficient on the airfoil obtained numerically and computationally are shown in Figure 14. The profile with deflection $\delta = 10°$ and angle of attack $\alpha = 4°$ was chosen to serve as a comparison to the blue curve called Hinged-Flap. It is possible to note the similarity between the curves, even though a more negative pressure is observed on the extrados, which explains why in these conditions the lift generated is slightly greater than that obtained by the author.

7.3 KUMAR AND KUMAR (2013)

Kumar and Kumar (2013) performed numerical simulations of the aerodynamic flow over a NACA 0012 airfoil with a plain flap, analyzing different angles of attack and deflection angles. Results for the coefficients of lift (C_l) and drag (C_d) are compared for four values of flap deflection ($\delta = 0°$, $5°$, $10°$ and $15°$) and angle of attack ($\alpha = 0°$, $4°$, $8°$ and $12°$). The authors used the $k - \epsilon$ turbulence model, a kinematic viscosity $\nu = 1.78 \cdot 10^{-5}\ m^2/s$ and a velocity entering the computational domain $U_\infty = 25\ m/s$ which results in a Reynolds number $Re = 1.7 \cdot 10^6$.

In order to repeat the results, the same boundary conditions and flow properties were used, but the Spalart Almarras tubulence model was selected again, as it better aligns with the scope of this work. In Figure 15, the lines represent the results obtained by OpenFOAM® while the diamonds show the author's results. It can be seen that the results were similar to the author's in terms of lift coefficient, while in terms of drag, the simulation proved to be more accurate for moderate angles of attack.

Figure 15 – (a) Lift and (b) Drag coefficients results obtained in the present work and by Kumar and Kumar (2013)



(a) (b)

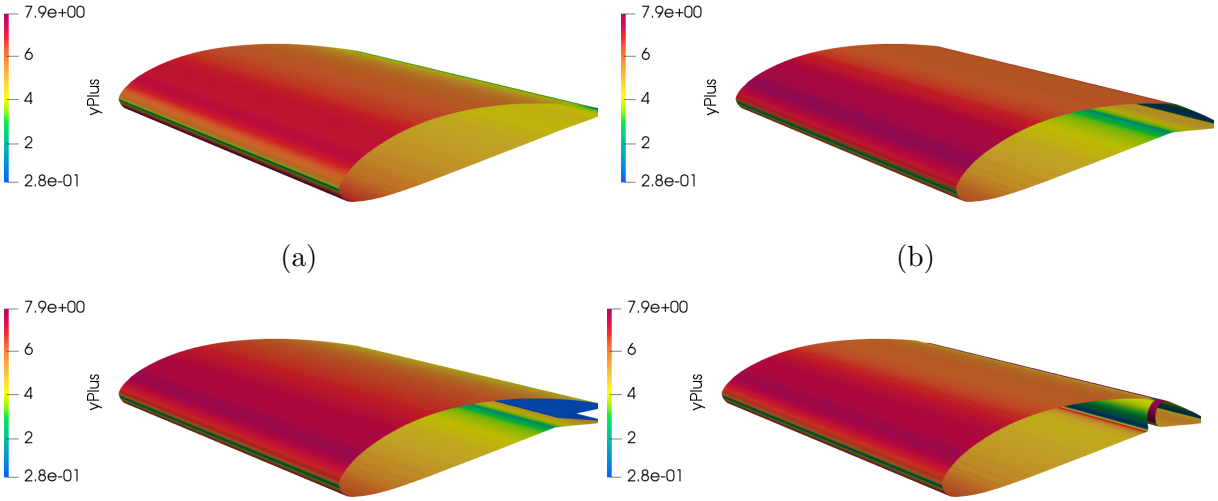
Source: (KUMAR; KUMAR, 2013).

8 RESULTS

8.1 MESH REFINEMENT TEST

The meshes used for the simulations in this work were generated using the methodology described in section 5, using minimum quality requirements that solved highly skewed, non-orthogonal or negative volume cells. As previously mentioned, the variable y^+ is an important dimensionless number that represents the size of the first element near the wall. Figure 16 shows the distribution of this number over the surfaces of some airfoils; for the sake of brevity, they can be considered representative of the distribution of y^+ for all the simulations carried out. It can be seen that its value remains lower than 7 for most of the surface, although it exceeds this value for small portions of the leading edge.

Figure 16 – y^+ distribution along various airfoil and high-lift surfaces.



Additionally, mesh independence tests were carried out for those flap configurations to ensure that the results analyzed were not a function of mesh refinement. To do this, Figure 17 shows the lift and drag coefficient results for the simulations of the flow over the clean airfoil, with a plain flap for different angles of attack. Below, in Table 2, mesh properties such as the number of cells and layers of elements near the airfoil are shown for comparison. It can be concluded that the mesh used has results close enough to those obtained with the refined mesh, but with lower computational cost and simulation time.

Figure 17 – Influence of mesh refinement in lift and drag coefficients for (a), (b) the clean airfoil and (c), (d) the plain flap.

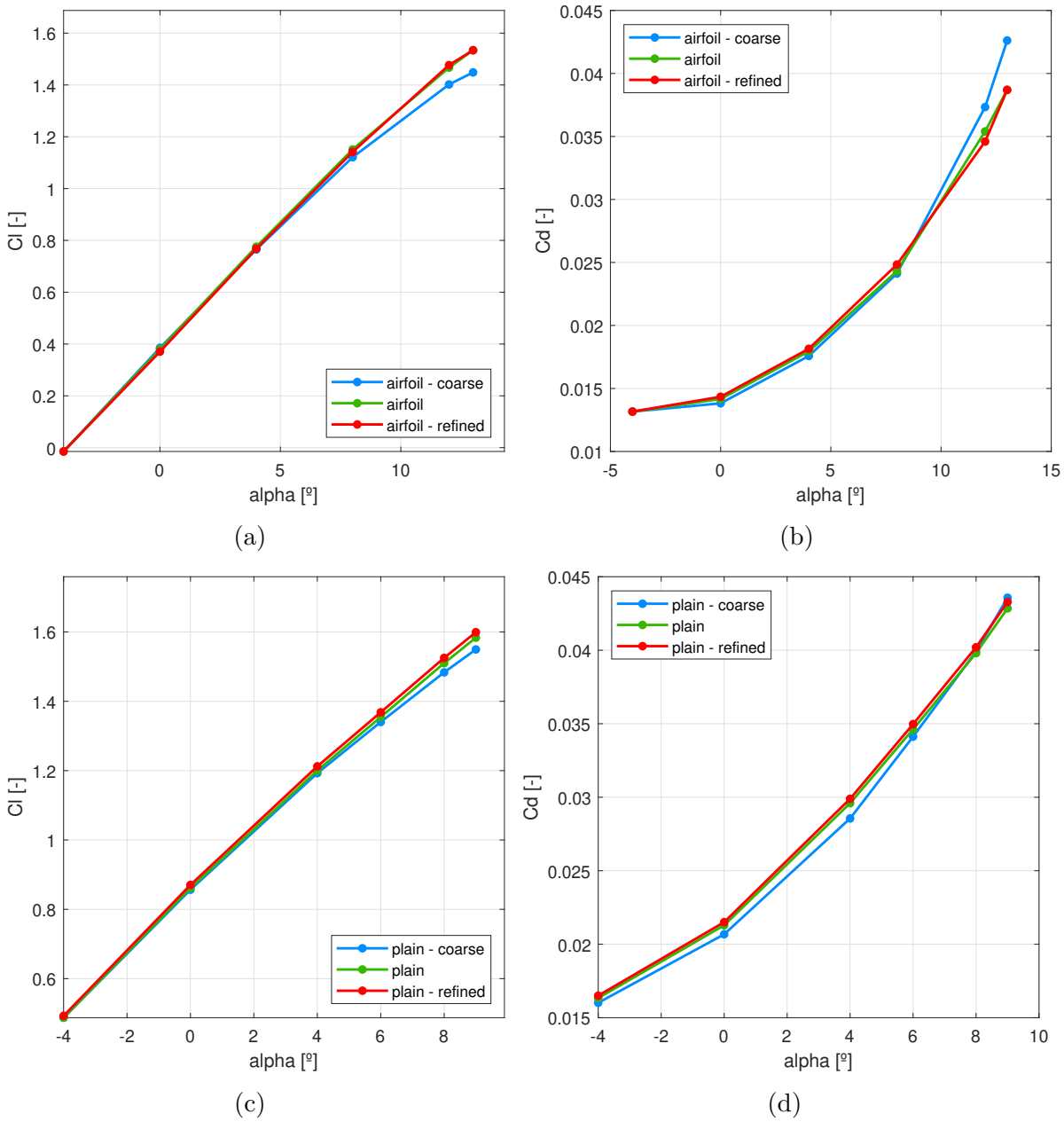


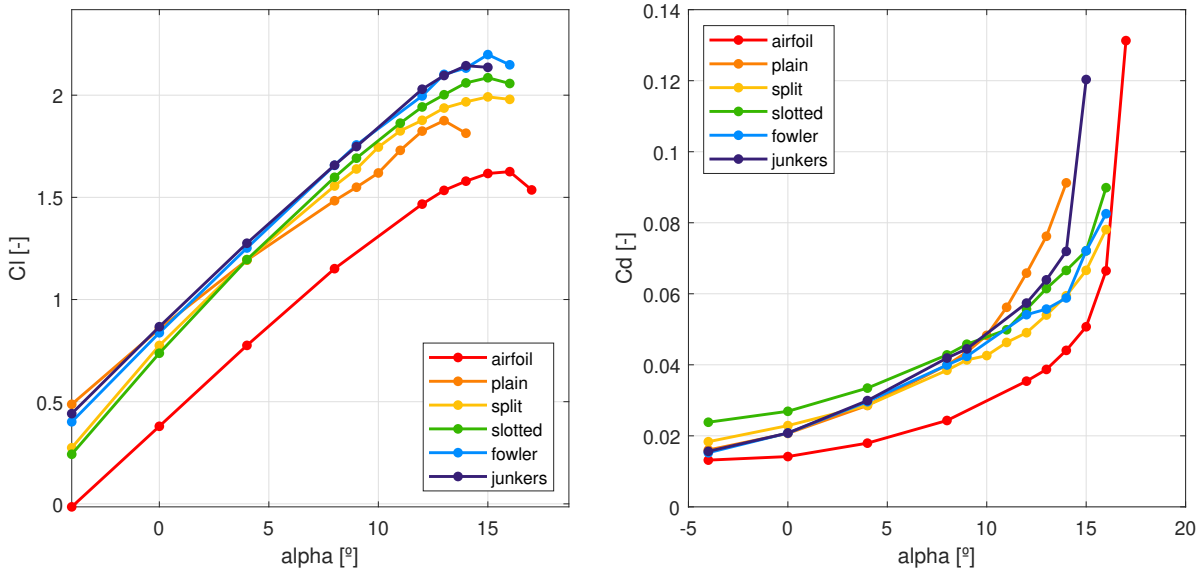
Table 2 – Properties of meshes subject to the independence test.

Mesh	Nº of cells	Nº of layers
Clean airfoil		
Coarse	440640	4
Medium	464113	5
Refined	1746817	9
Plain flap		
Coarse	424451	4
Medium	780796	5
Refined	823752	9

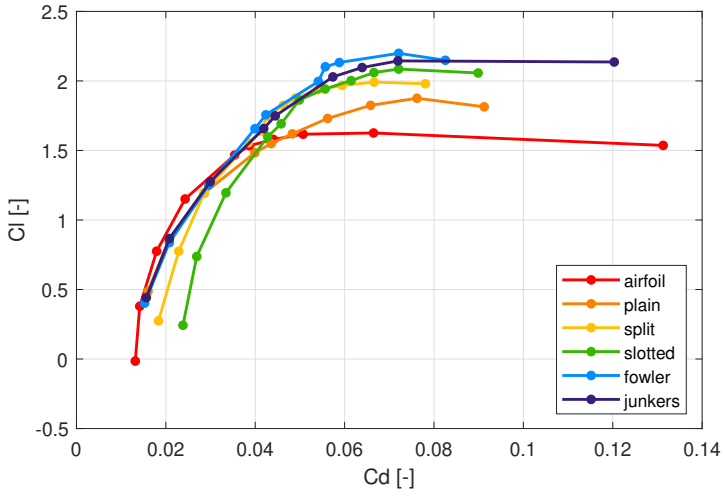
8.2 HIGH-LIFT CONFIGURATION COMPARISON

The results are compared with the control group, the clean NACA4415 airfoil, designated as *"airfoil"*. A compilation of the results of the lift and drag coefficients for the NACA4415 airfoil equipped with different flap configurations is shown in Figure 18, where each type of flap is identified by a color. It is possible to verify the behavior of the coefficients for the clean airfoil, the lift has a linear region with a slope $C_{l\alpha} = 5.52\ rad^{-1}$, a maximum coefficient $C_{lmax} = 1.626$ which occurs at angle $\alpha = 16°$. For drag, it has its minimum value for α between $-4°$ and $0°$, increasing along with the angle of attack.

Figure 18 – (a) Lift and (b) Drag coefficients results for the clean airfoil and different flap configurations as a function of the angle of attack. (c) Lift coefficient as a function of Drag coefficient.



(a) (b)



(c)

Figure 19 – Velocity field of the flow over the clean airfoil for (a) $\alpha = 0°$, (b) $\alpha = 4°$, (c) $\alpha = 8°$, (d) $\alpha = 12°$ and (e) $\alpha = 14°$.

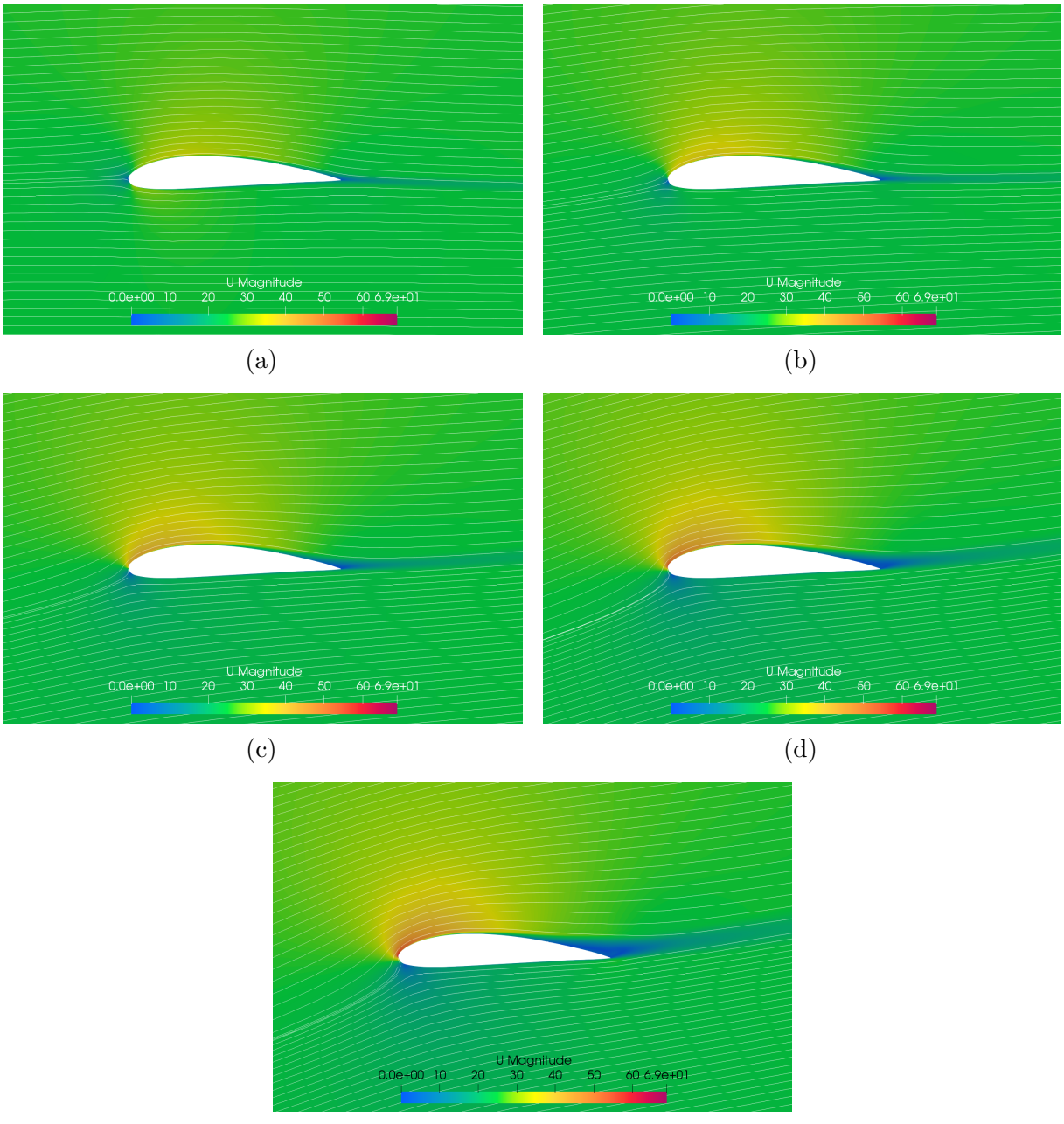
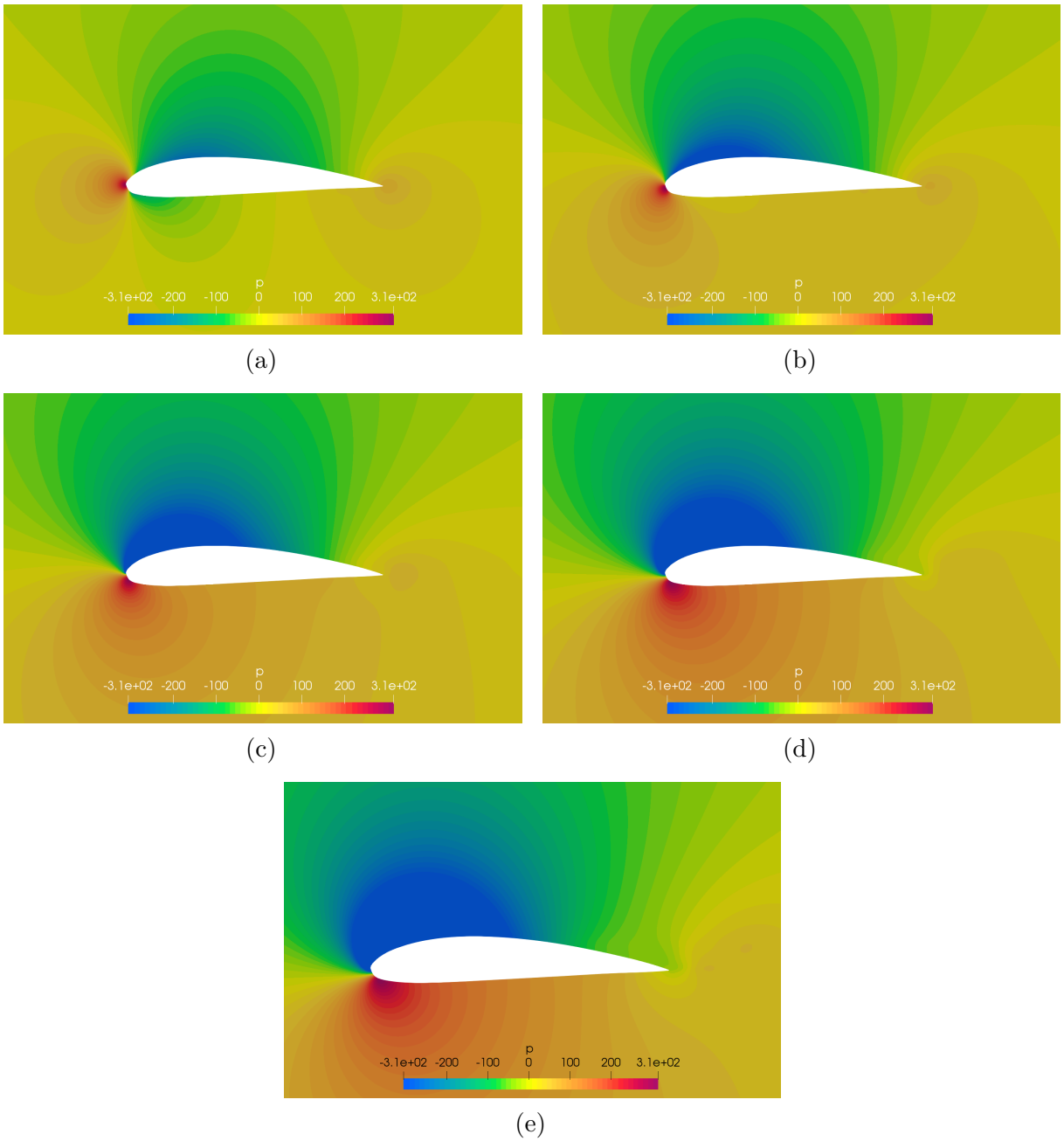


Figure 19 shows the velocity fields of the flow around the airfoil for different angles of attack. It can be seen that a stagnation point occurs at the leading edge of the airfoil, which moves towards the surface underneath the airfoil as the angle of attack increases. Similarly, the velocity gradient observed on the upper surface increases. When $\alpha = 0°$, the flow remains adhered to almost the entire surface, but begins to detach up until when $\alpha = 15°$ it detaches near the leading edge.

Figure 20 shows the pressure fields for the same AOAs. The pressure contours show regions of high pressure that follow the location of the stagnation points, and the region

Figure 20 – Kinematic pressure field of the flow over the clean airfoil for (a) $\alpha = 0°$, (b) $\alpha = 4°$, (c) $\alpha = 8°$, (d) $\alpha = 12°$ and (e) $\alpha = 14°$.



(a) (b)

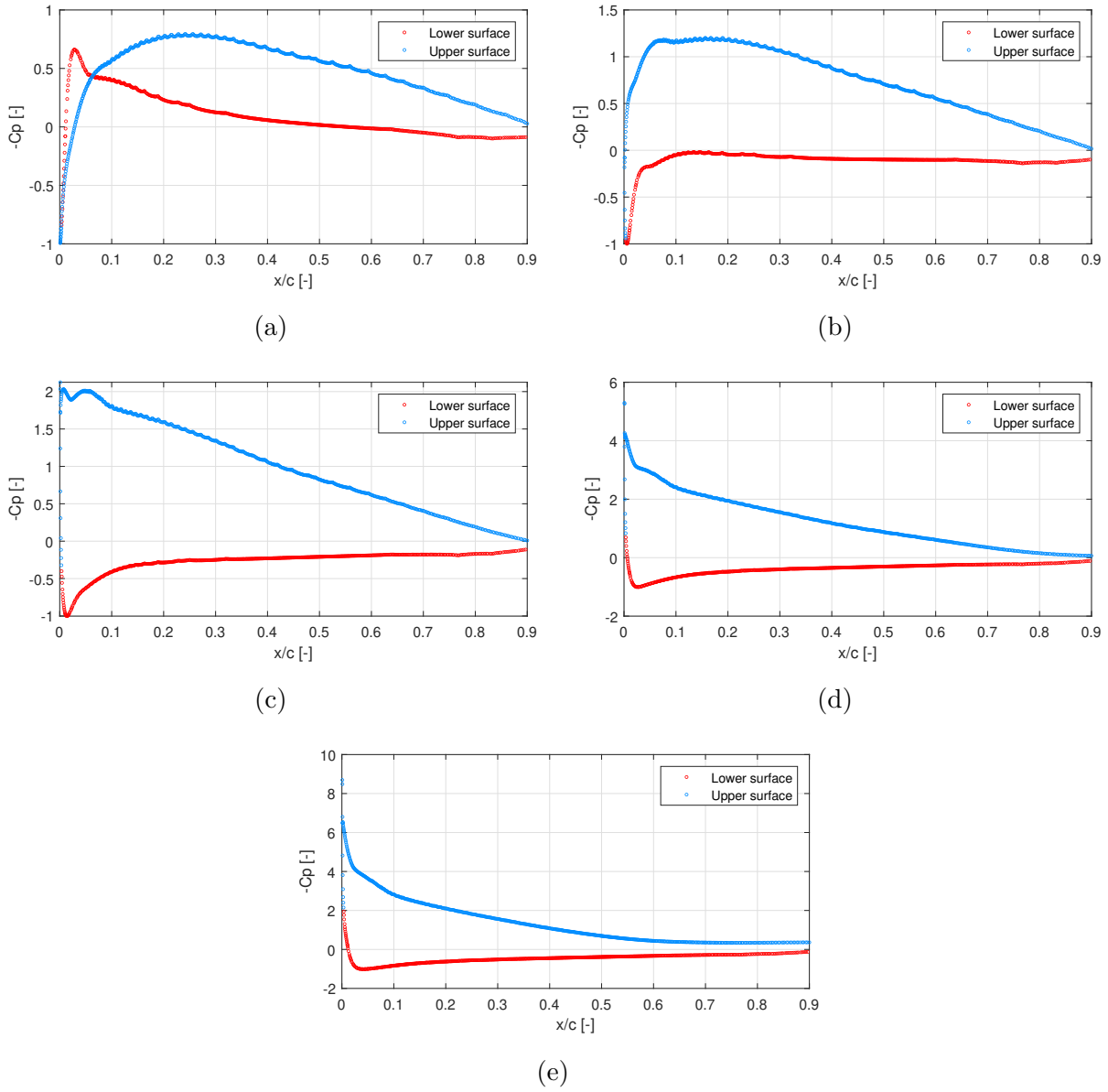
(c) (d)

(e)

of low pressure over the upper surface decreases with the detachment of the boundary layer while its gradient becomes increasingly abrupt. The pressure difference along the wing is the mechanism by which lift is transferred to the wing due to the bending of the flow, this behavior will be observed throughout this work. A similar behavior is found in the distribution of the pressure coefficient in Figure 21. For smaller angles of attack, the pressure difference between the upper and lower surfaces is small, generating little lift; as α increases, the pressure gradient intensifies.

As a result of the simulations, it can be seen that for this range of Reynolds numbers, lift is generated mainly due to pressure forces, while drag has similar contributions from

Figure 21 – Pressure coefficient distribution along the clean airfoil for (a) $\alpha = 0°$, (b) $\alpha = 4°$, (c) $\alpha = 8°$, (d) $\alpha = 12°$ and (e) $\alpha = 16°$.



(a) (b)

(c) (d)

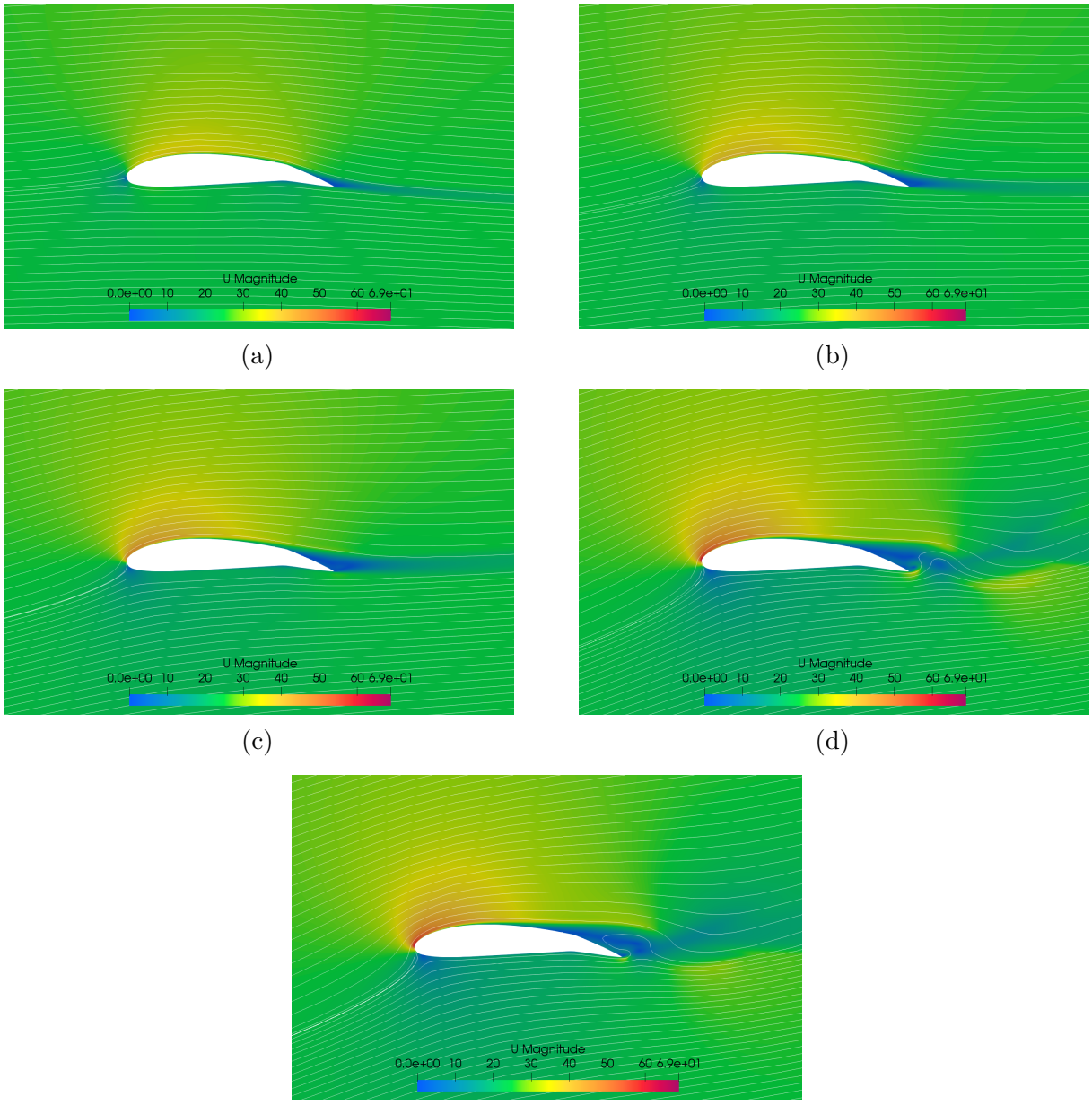
(e)

both viscous and pressure forces, so by looking at the pressure field, it is generally possible to determine the magnitude of the lift force, but not much can be said about drag.

8.2.1 Plain flap

The lift and drag coefficients for the plain flap are identified by the color orange and the label *"plain"* in Figure 18. It can be seen that, as with the hypothesis presented earlier, the lift generated is greater as the flap deflects, while the stall angle observed is smaller, close to 13°. The slope of the observed linear region is $C_{l\alpha} = 4.41\ rad^{-1}$, and the maximum lift coefficient $C_{lmax} = 1.884$.

Figure 22 – Velocity field of the flow over the airfoil with plain flap for (a) $\alpha = 0°$, (b) $\alpha = 4°$, (c) $\alpha = 8°$, (d) $\alpha = 13°$ and (e) $\alpha = 14°$.

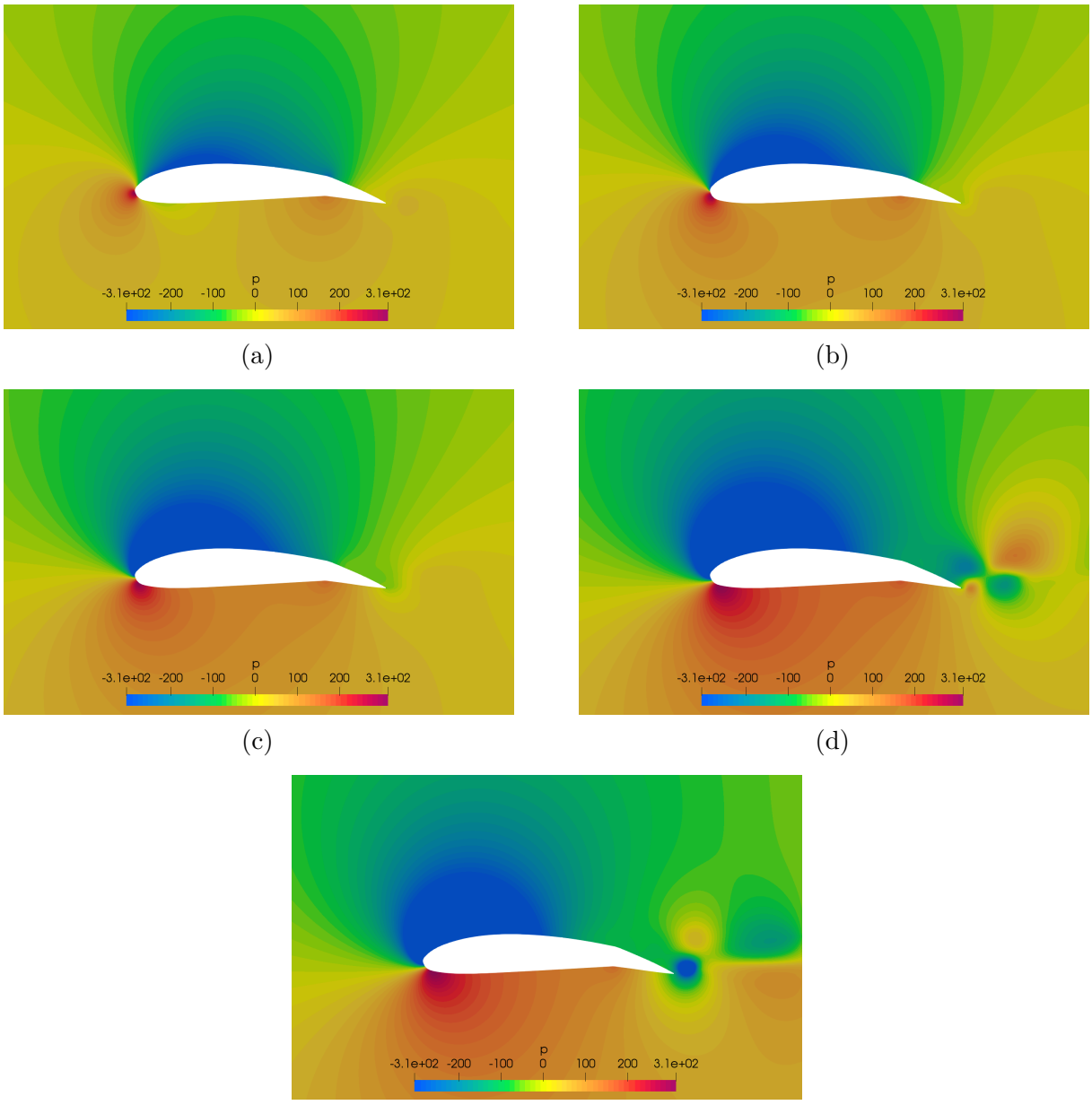


(a) (b) (c) (d) (e)

The increase in the maximum lift coefficient compared to the clen airfoil was $\Delta C_{lmax} = 0.258$, a result close to that found experimentally by Cahill (1949) of $\Delta C_{lmax} = 0.235$. The author analyzed airfoils from the NACA family for a range of Reynolds numbers $Re = 6 \cdot 10^5$ and with flap chords equal to 20% and 30% of the airfoil length. Meanwhile, the increase in the drag coefficient generated with flap deflection is to be expected and is more evident for steeper attack angles.

Figure 22 shows the velocity field for the simulations carried out on the plain flapped airfoil. It is possible to observe the same behaviors pointed out in the airfoil without deflection, namely, the stagnation point and the region of high velocity due to

Figure 23 – Kinematic pressure field of the flow over the airfoil with plain flap for (a) $\alpha = 0°$, (b) $\alpha = 4°$, (c) $\alpha = 8°$, (d) $\alpha = 13°$ and (e) $\alpha = 14°$.

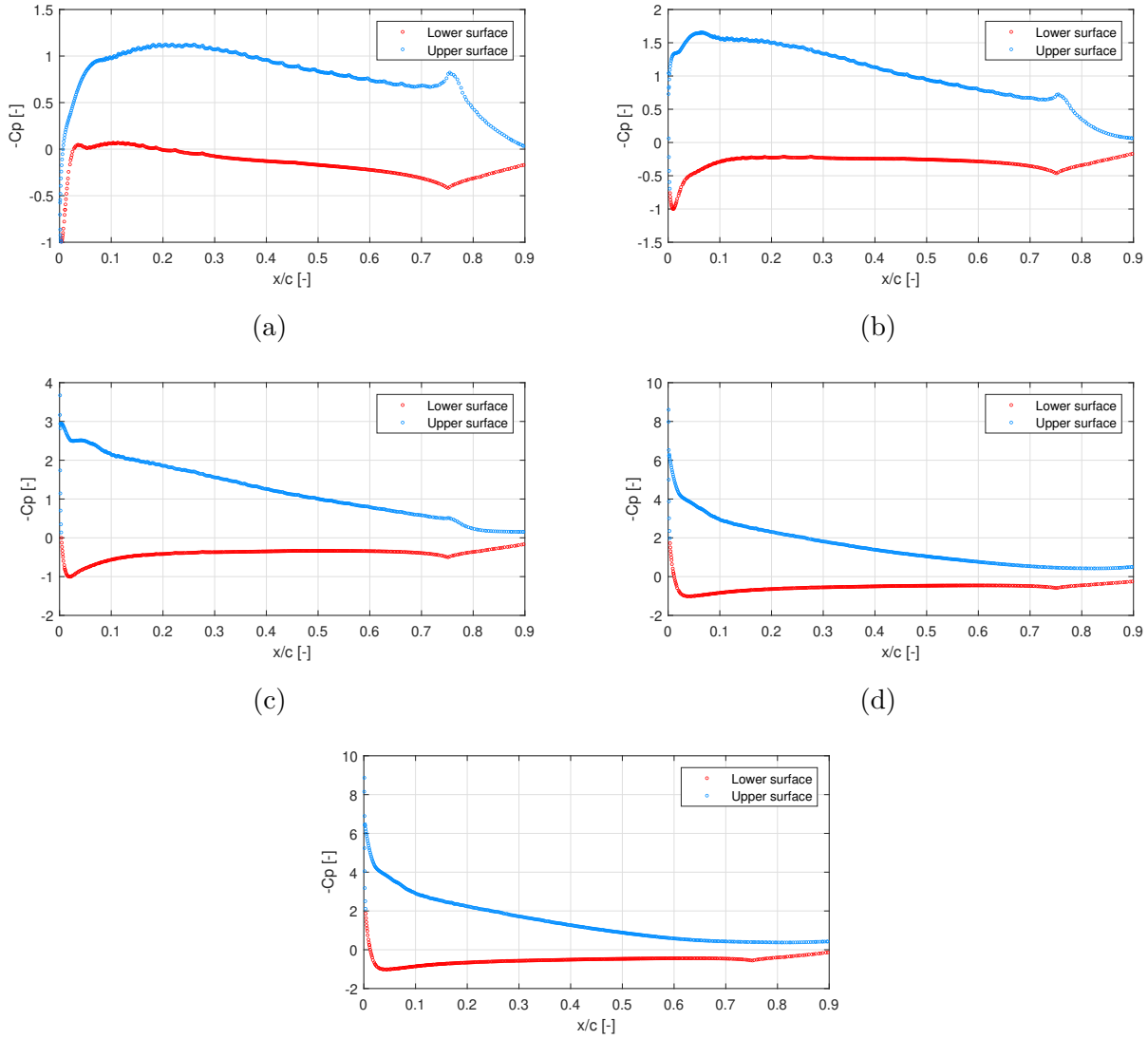


(a) (b) (c) (d) (e)

the deflection of the flow to follow the geometry of the surface, known as upwash. The detachment of the boundary layer approaches the leading edge for much smaller angles of attack.

The behavior of the pressure field is shown in Figure 23, presenting more pronounced pressure gradients than the previous case, both negative and positive, which explains the greater generation of lift and drag for all angles of attack. Taking a more detailed view, the pressure coefficient distribution in Figure 24 highlights the difference in pressure between the lower and upper surfaces, explaining the high-lift even for small angles of attack. For smaller inclinations, it is possible to see a pressure peak near 75 % of the airfoil chord,

Figure 24 – Pressure coefficient distribution along the airfoil with plain flap for (a) $\alpha = 0°$, (b) $\alpha = 4°$, (c) $\alpha = 8°$, (d) $\alpha = 13°$ and (e) $\alpha = 14°$.



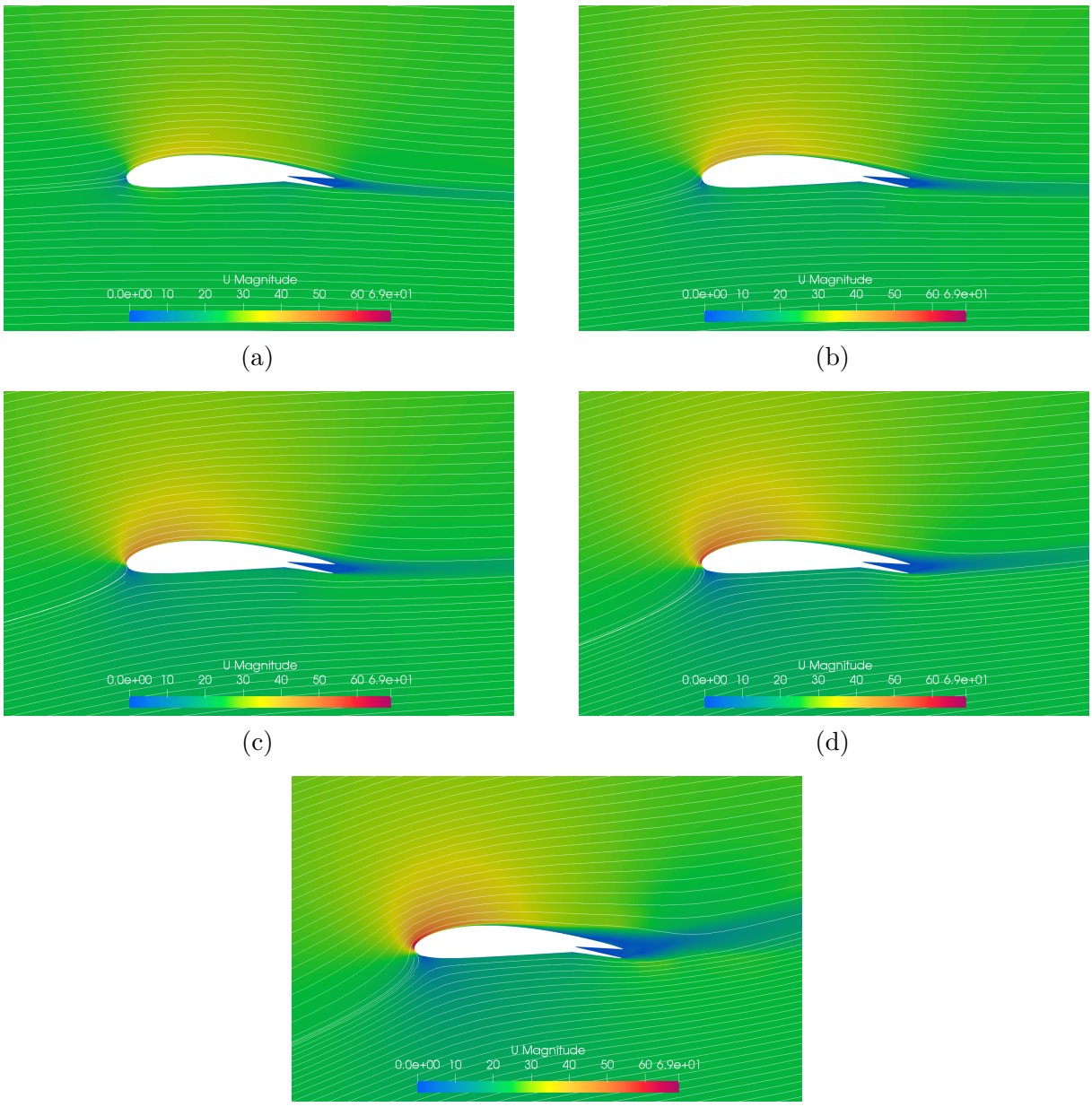
on both surfaces. The peak is due to the sudden change in surface inclination due to the deflection of the flap, which causes a local bending in the flow, increasing the velocity locally. When α is higher, this phenomenon is no longer observed with such magnitude, since the boundary layer detachment extends beyond the flap's hinge point.

8.2.2 Split flap

As for the split flap, in Figure 18 it is represented by the color yellow and the label *split*. In terms of the lift generated, it can be seen that its performance is better than the previous case. Despite generating less lift for low and negative angles, the split flap has a steeper lift curve, $C_{l\alpha} = 6.08\ rad^{-1}$, which results in higher lift levels for larger angles of attack. In addition, the stall angle was greater than when using the plain flap, the lift

curve reaching its maximum $C_{lmax} = 1.981$ which occurs at angle $\alpha = 15°$. As pointed out earlier, the split flap does generate greater drag at low angles of attack, but it proved to be more efficient than the plain flap for moderate angles of attack. It is intuitive to conclude that for larger flap deflections the drag generated would be much greater at small angles of attack, and could act as a spoiler in landing conditions.

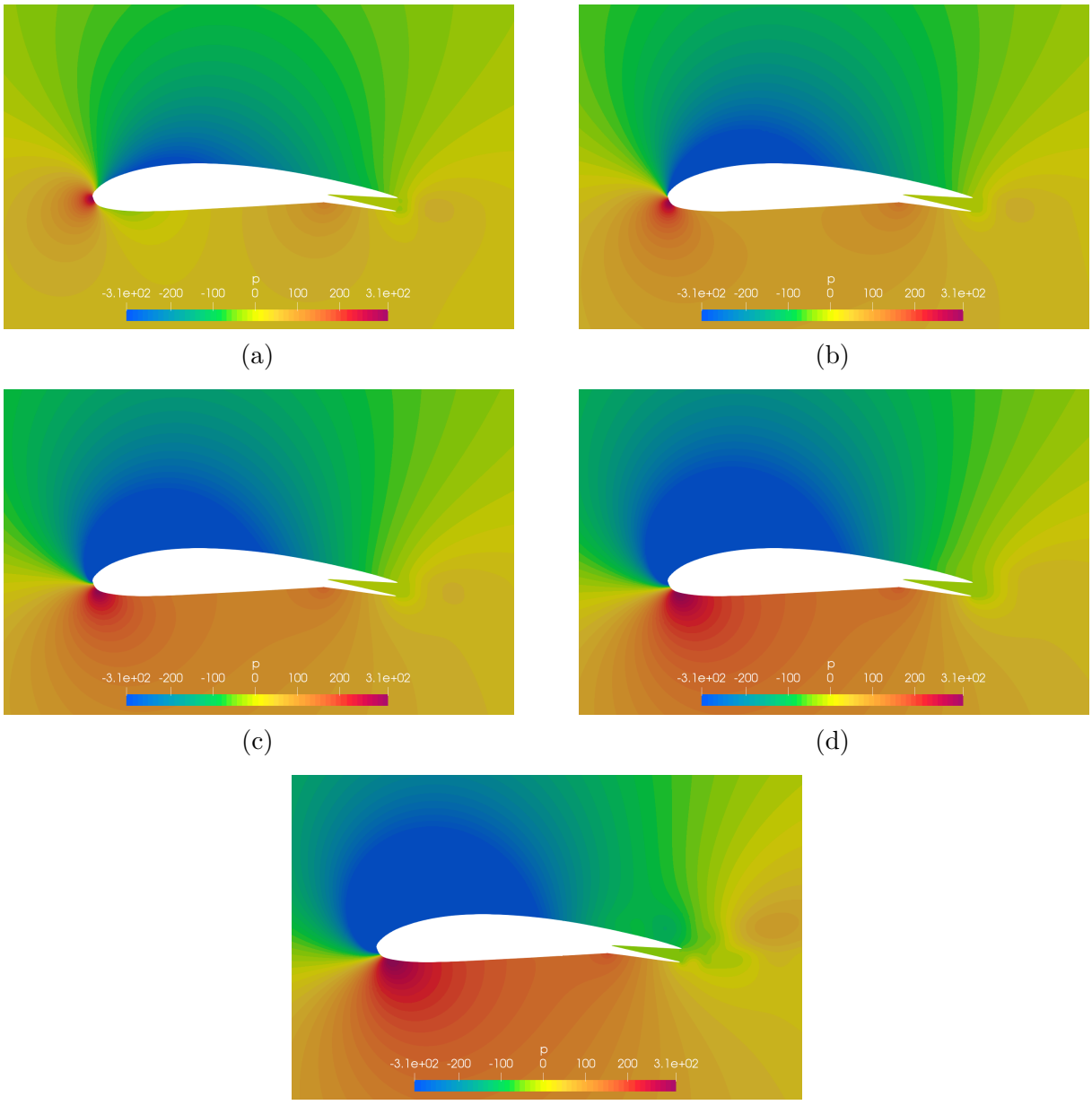
Figure 25 – Velocity field of the flow over the airfoil with split flap for (a) $\alpha = 0°$, (b) $\alpha = 4°$, (c) $\alpha = 8°$, (d) $\alpha = 12°$ and (e) $\alpha = 15°$.



(a) (b) (c) (d) (e)

Compared to the clean airfoil, the split flap generates an increase in maximum lift of $\Delta C_{lmax} = 0.367$, compared to the results extrapolated from the work by Gudmundsson (2022) of $\Delta C_{lmax} = 0.383$ for split flaps coupled to NACA family airfoils analyzed in a lower Reynolds range, $Re = 6 \cdot 10^5$ with a chord ratio equal to 0.2 and 0.3. The split flap, unlike

Figure 26 – Kinematic pressure field of the flow over the airfoil with split flap for (a) $\alpha = 0°$, (b) $\alpha = 4°$, (c) $\alpha = 8°$, (d) $\alpha = 12°$ and (e) $\alpha = 15°$.



(a) (b)

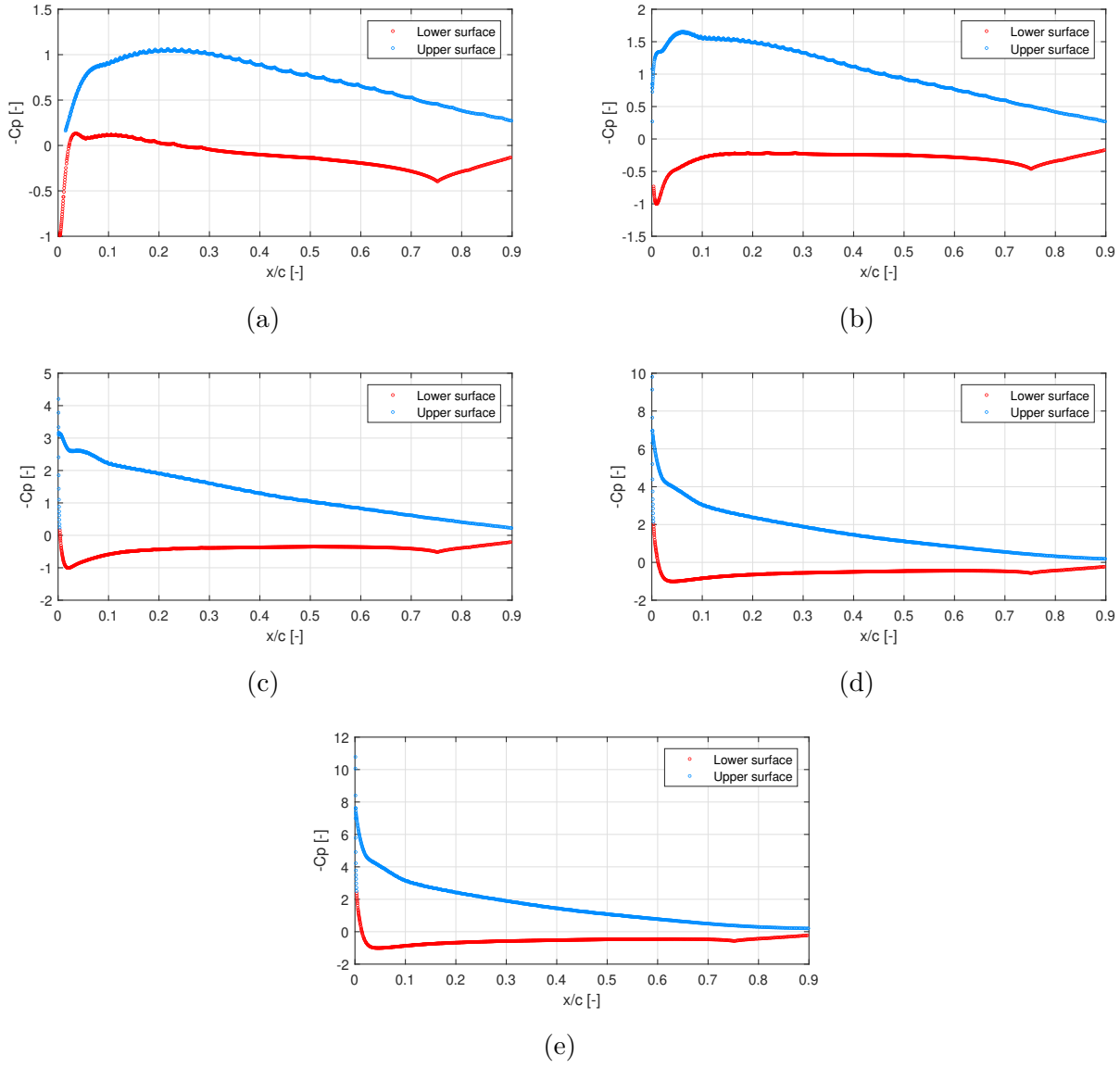
(c) (d)

(e)

the other flaps analyzed in this paper, was not studied at its optimum deflection between 60° and 70°. However, in order to preserve the study's original intention of comparing different airfoil configurations in similar physical conditions, the deflection angle was chosen to be 10°, since simulations of other configurations would not be representative of normal flight conditions for larger angles.

In the velocity field of Figure 25 it is possible to observe the behavior of the flow at the trailing edge of the airfoil, in addition to the leading edge phenomena already mentioned in the previous cases. Because the deflection of this type of flap occurs only on the lower surface of the airfoil, the flow is not significantly deflected at low angles of

Figure 27 – Pressure coefficient distribution along the airfoil with split flap for (a) $\alpha = 0°$, (b) $\alpha = 4°$, (c) $\alpha = 8°$, (d) $\alpha = 13°$ and (e) $\alpha = 14°$.



(a)

(b)

(c)

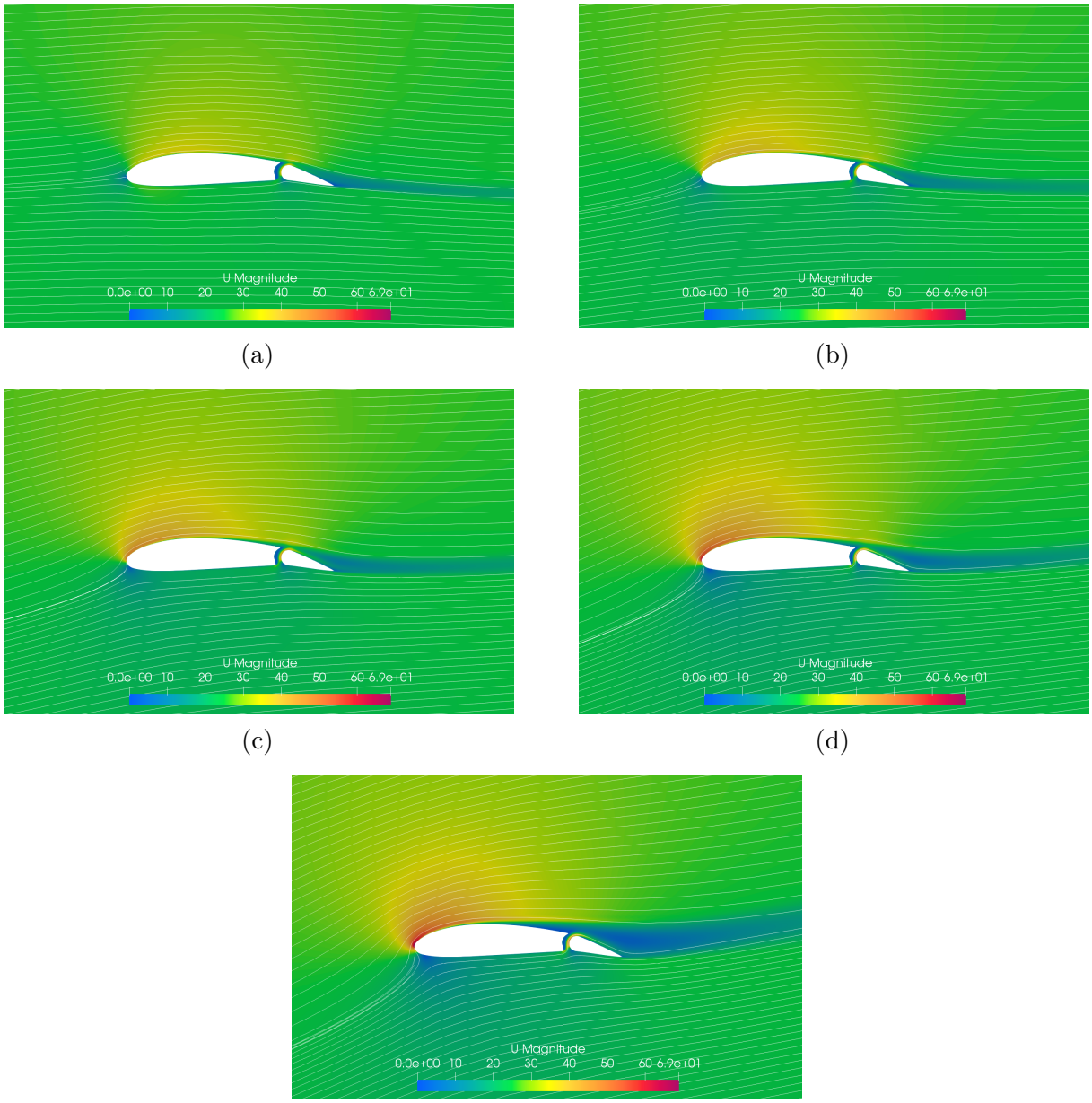
(d)

(e)

attack, generating little downwash and less lift than the plain flap, for example. However, a positive aspect to note is that as the upper surface does not change direction abruptly, the boundary layer detachment occurs at much greater angles, making it possible to delay the stall. In addition, it is possible to see a big separation between the flap blades at the trailing edge and the wake behind the airfoil. The pressure contour in Figure 26, together with the C_p distribution in Figure 27 back up the previously explained behavior. The presence of an unchanged top surface with a smooth transition prevents the formation of low-pressure peaks near the flap's hinge line. For larger angles of attack, the negative pressure gradient on the upper surface in the first 25% of the chord results in greater lift.

8.2.3 Slotted flap

Figure 28 – Velocity field of the flow over the airfoil with slotted flap for (a) $\alpha = 0°$, (b) $\alpha = 4°$, (c) $\alpha = 8°$, (d) $\alpha = 12°$ and (e) $\alpha = 16°$.



(a) (b)

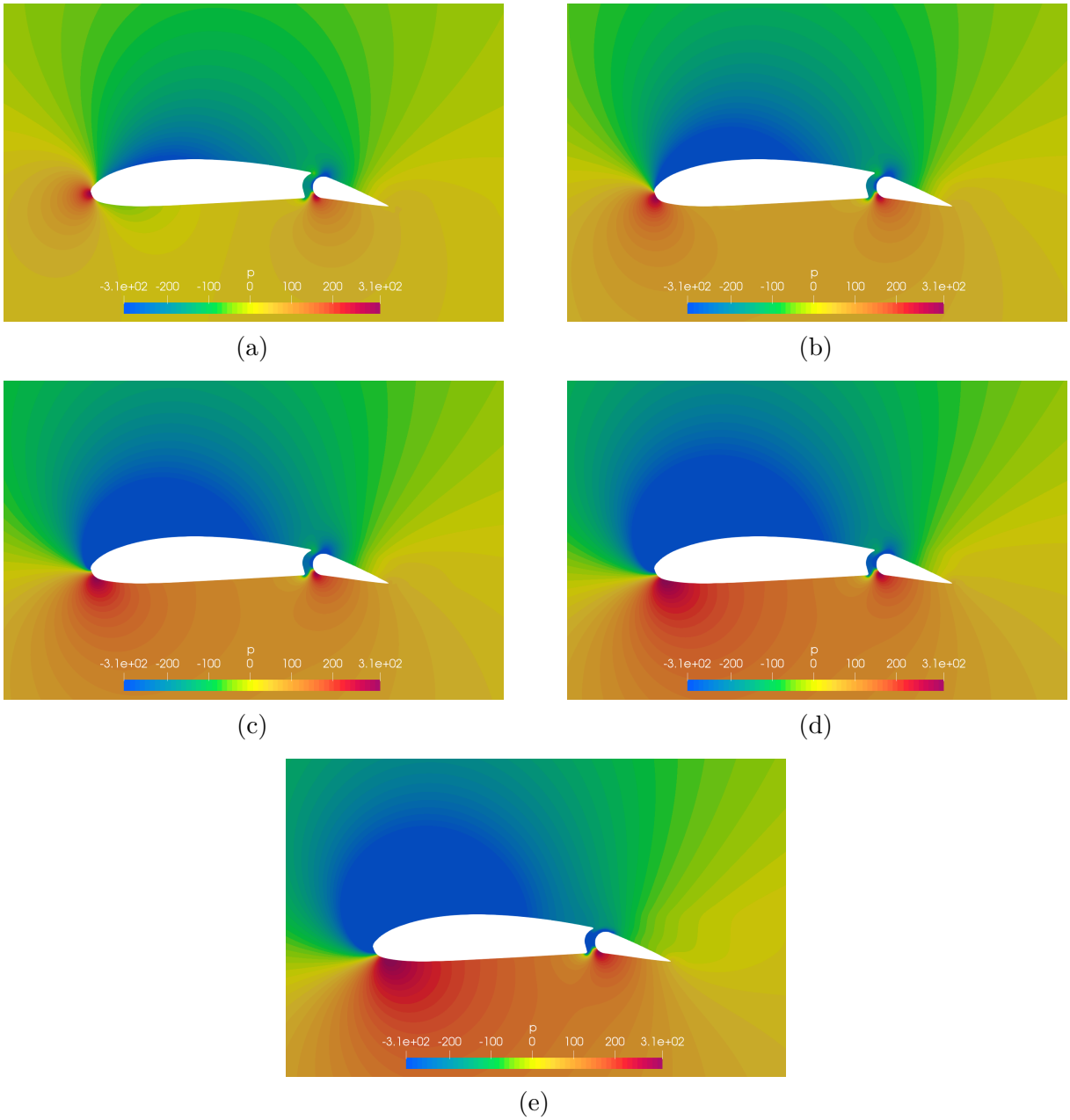
(c) (d)

(e)

The aerodynamic coefficients of the flow over the slotted flap are identified with the label *slotted* and the color green in Figure 18. When the lift curve is analyzed, the behavior is very similar for both the plain flap and the split flap with the same deflection angle. However, as expected, the stall angle is greater than the first case described, this time peaking at $\alpha = 15°$ and reaching a higher level of lift than both devices shown, with $C_{lmax} = 2.085$. With a slope almost identical to that of the split flap, $C_{l\alpha} = 6.07\ rad^{-1}$, it can be seen that the effect of the slot is comparable to that of the deflection of the lower surface of the flap. As for drag, this type of flap showed high levels at low angles of attack

but was close to the other configurations, reaching a maximum aerodynamic efficiency of $L/D = 37.43$ when $\alpha = 8°$.

Figure 29 – Kinematic pressure field of the flow over the airfoil with slotted flap for (a) $\alpha = 0°$, (b) $\alpha = 4°$, (c) $\alpha = 8°$, (d) $\alpha = 12°$ and (e) $\alpha = 16°$.

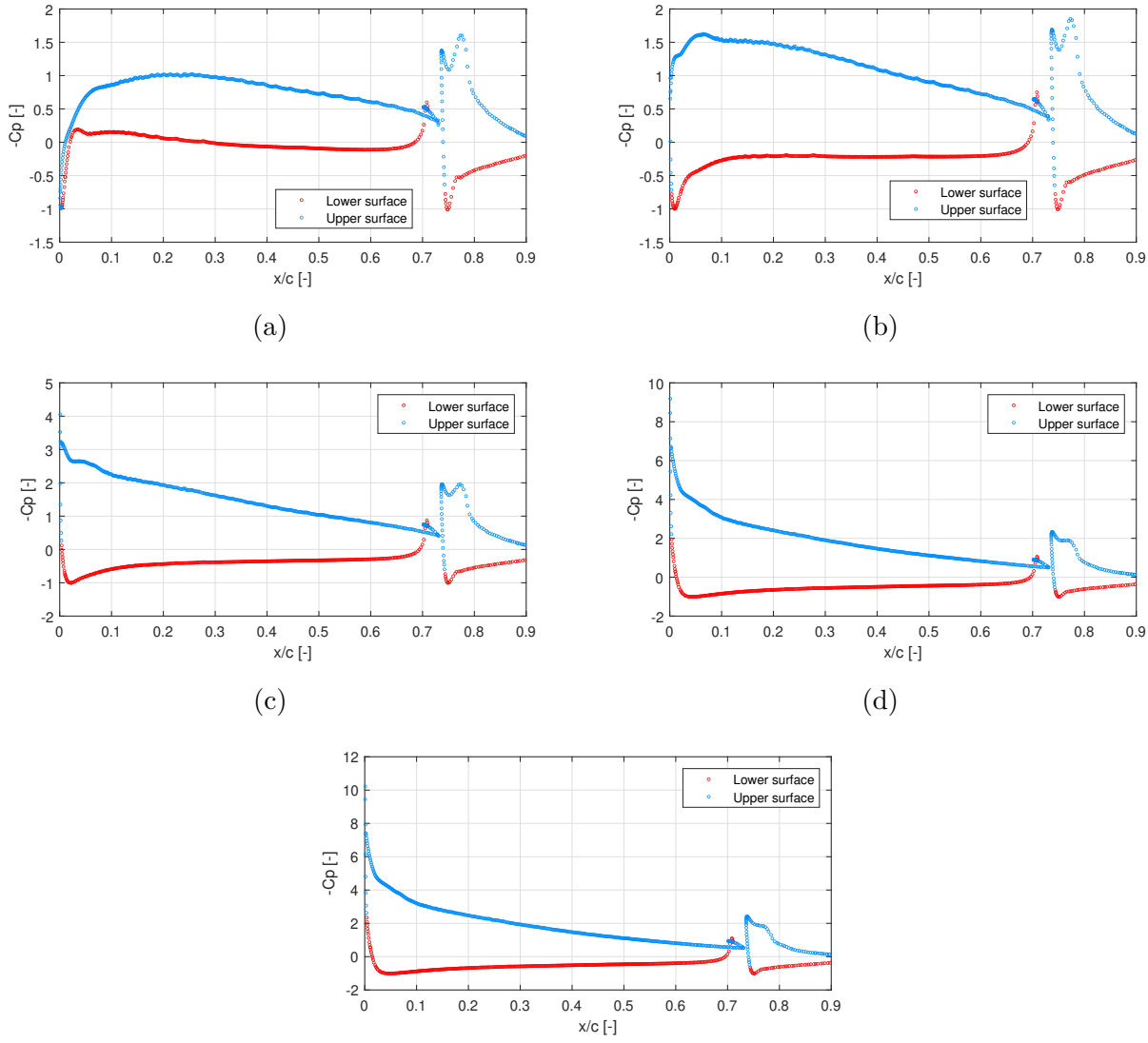


(a) (b) (c) (d) (e)

Figure 28 shows the velocity fields together with the flow current lines for the slotted flap. The behavior of the velocity at the leading edge is similar to the previous cases, but the influence of the presence of the slot on the flow is notable. Essentially the trailing edge of the airfoil acts as a second airfoil, the fluid flows around it, creating a stagnation point on the lower surface and a region with high velocities where the fluid accelerates and curves its trajectory to follow the curvature of the surface. Together with the results of the coefficient of lift, it is possible to understand why the force generated is

lower at smaller angles of attack, the downwash generated is lower compared to the plain flap at a zero angle of attack. However, as the angle of incidence increases, it can be seen that the detachment of the boundary layer, represented by the region with zero mean velocity, is delayed by the insertion of fluid from the lower region to the upper surface of the flow.

Figure 30 – Pressure coefficient distribution along the airfoil with slotted flap for (a) $\alpha = 0°$, (b) $\alpha = 4°$, (c) $\alpha = 8°$, (d) $\alpha = 13°$ and (e) $\alpha = 14°$.



(a) (b)

(c) (d)

(e)

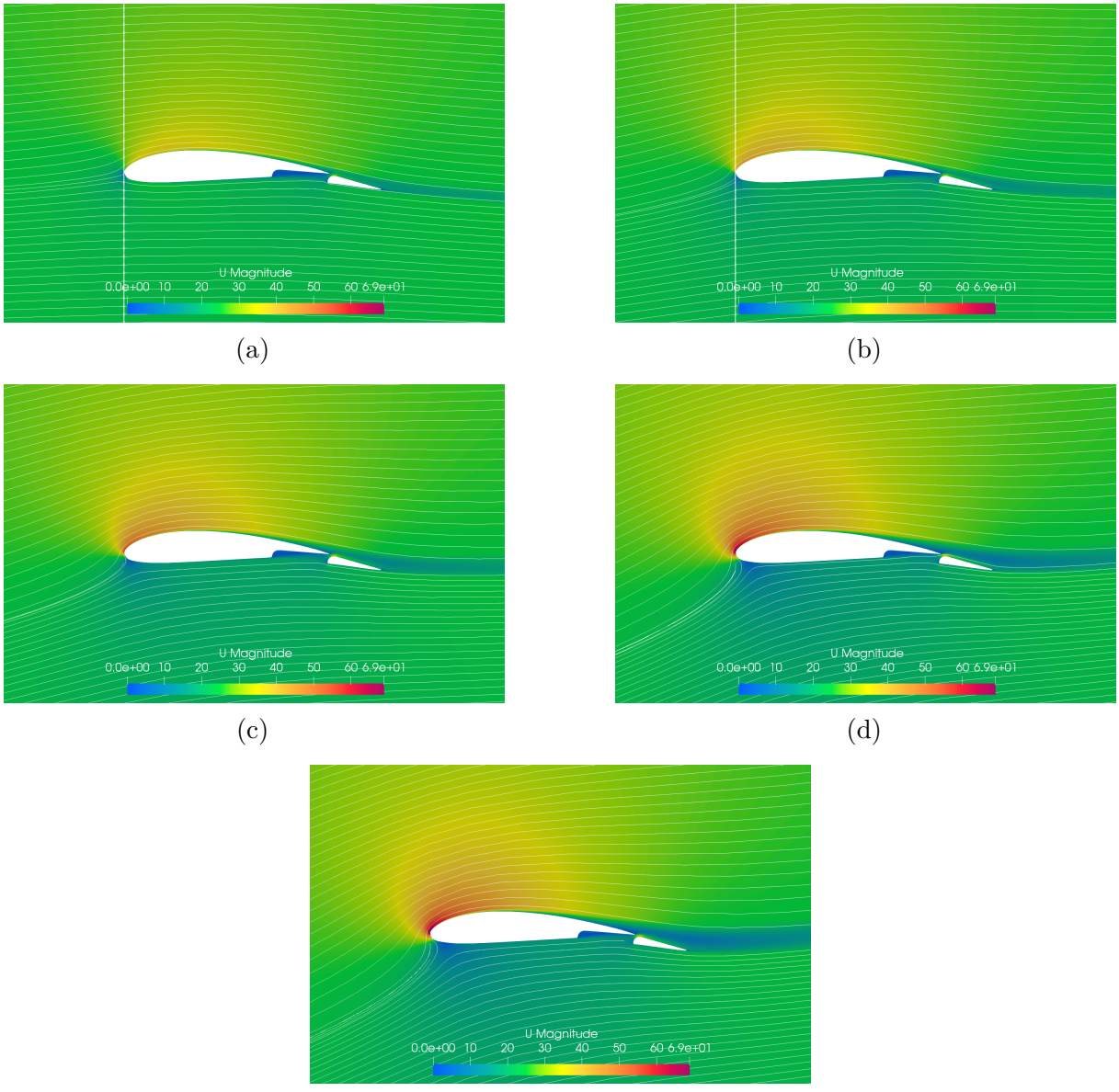
In Figure 29 the pressure contours are shown for the same flow. The figure shows that the presence of the slot causes a smaller pressure difference between the regions below and above the airfoil, this is due to the exchange of fluids between the two regions, which tends to balance the pressure. However, there is still a pressure gradient between the surfaces, and once again there is a region of high pressure at the location of the stagnation point, which contributes to the generation of lift. It is possible to observe the pressure

gradient in the slope as the flow crosses the channel and enters the low-pressure region.

The graph in Figure 30 quantitatively shows the information presented above. For low angles of attack, higher pressure levels are found on the trailing edge at 75% of the airfoil chord, after the slot, on both the upper and lower surfaces. As the angle of attack increases, the contribution to lift generation of the first 25% of the chord increases greatly while the pressure levels on the flap remain constant. In general, for high angles of attack, the slot plays the role of re-energizing the velocity boundary layer and preventing flow separation more significantly than it increases lift generation.

8.2.4 Fowler flap

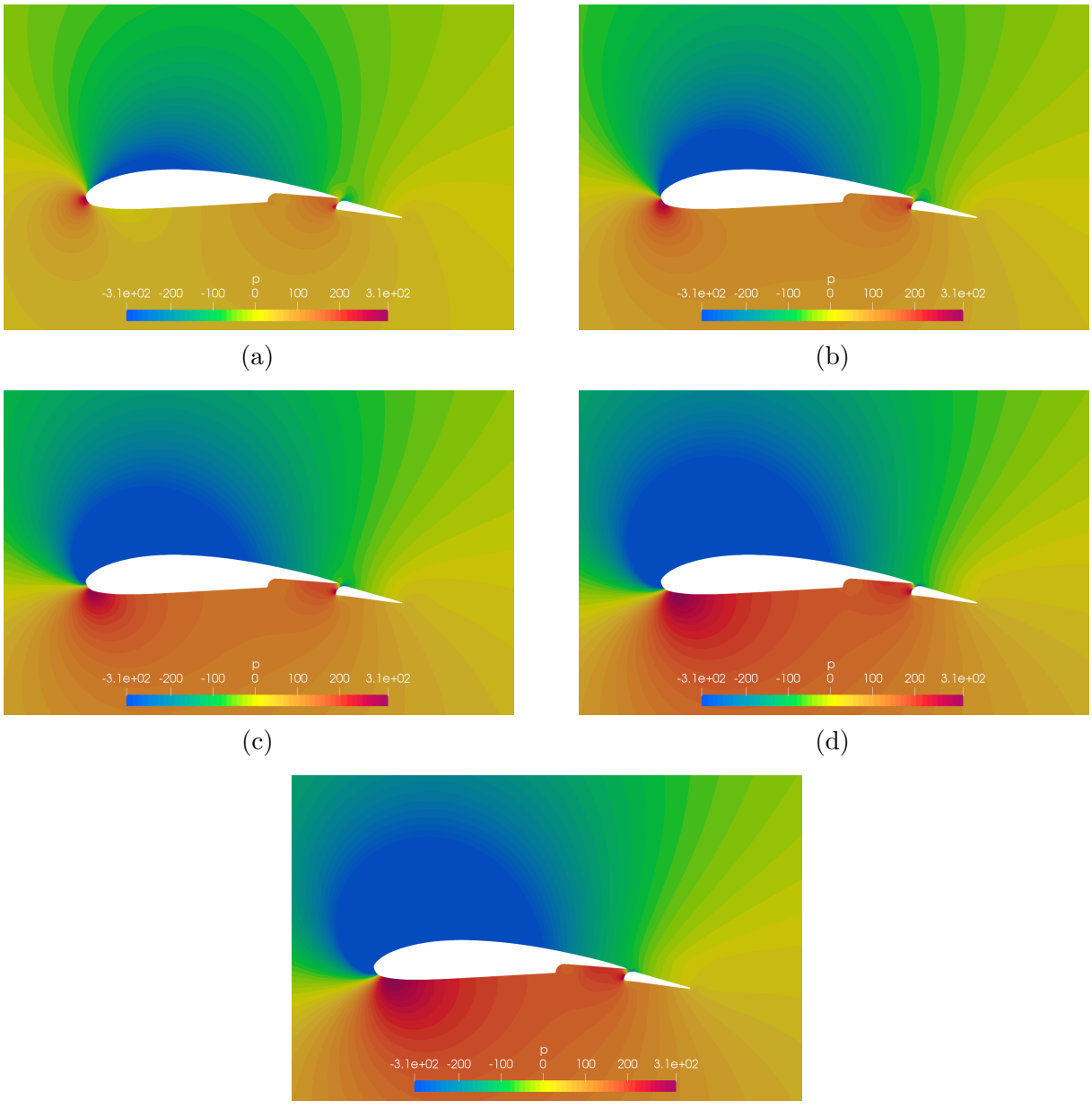
Figure 31 – Velocity field of the flow over the airfoil with fowler flap for (a) $\alpha = 0°$, (b) $\alpha = 4°$, (c) $\alpha = 8°$, (d) $\alpha = 13°$ and (e) $\alpha = 14°$.



(a) (b) (c) (d) (e)

The lift coefficient curve of the fowler flap is shown in Figure 18, represented by the color blue. It is easy to see that, among the flap configurations analyzed, this is the one with the greatest potential for generating lift, with the highest C_l levels. This is due to the property of Fowler flaps of significantly increasing the chord of the airfoil in addition to rotation, keeping the flow adhered to the surface while it is deflected. As the planiform area of the airfoil essentially increases with the deflection of the flap, the reference area used to calculate the coefficients is not unitary, but must be 1.25.

Figure 32 – Kinematic pressure field of the flow over the airfoil with fowler flap for (a) $\alpha = 0°$, (b) $\alpha = 4°$, (c) $\alpha = 8°$, (d) $\alpha = 13°$ and (e) $\alpha = 14°$.



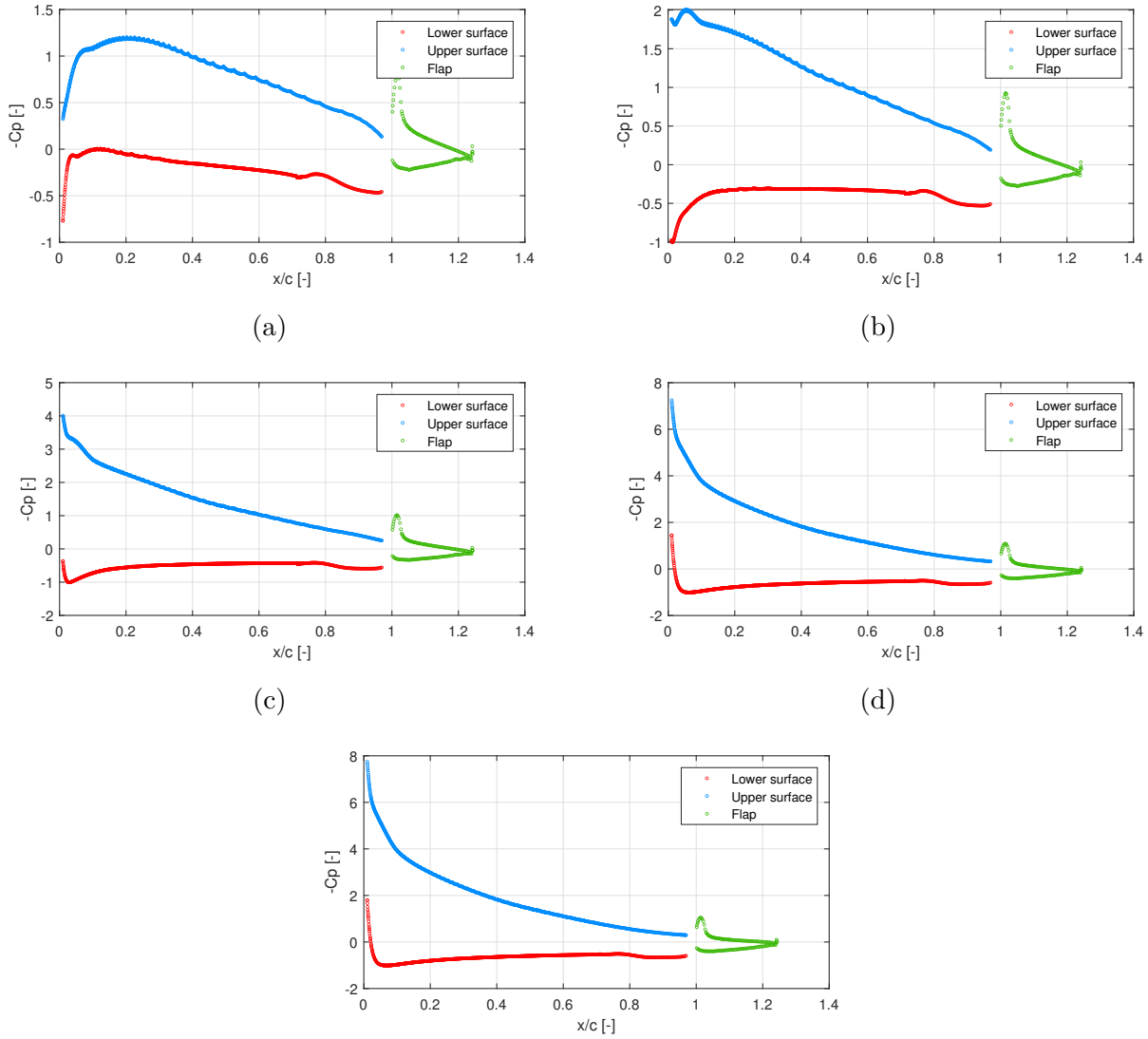
(a) (b)

(c) (d)

(e)

A stall angle of $\alpha = 15°$ is observed, but this generates the highest maximum lift coefficient, $C_{lmax} = 2.199$. The inclination is greater than in the previous cases,

Figure 33 – Pressure coefficient distribution along the airfoil with fowler flap for (a) $\alpha = 0°$, (b) $\alpha = 4°$, (c) $\alpha = 8°$, (d) $\alpha = 13°$ and (e) $\alpha = 14°$.



$C_{l\alpha} = 5.848\ rad^{-1}$, the change being due to the Fowler movement of rotation and translation of the flap. As for drag, it doesn't show significant values compared to other flaps, mainly due to the magnitude of the lift generated. This results in high aerodynamic efficiency, reaching a maximum of $L/D = 42.29$ when $\alpha = 4°$.

The streamlines in Figure 31 show a flow very similar to that of the slotted flap, where the gap between the main element and the flap acts as the slot to delay the detachment of the boundary layer. It is possible to observe the stagnation point and the bending region of the flow just as it occurred in the flow over the slot flap. Essentially, the flap acts as an extension of the airfoil, keeping the flow adhered to the surface and deflecting it further, generating more lift.

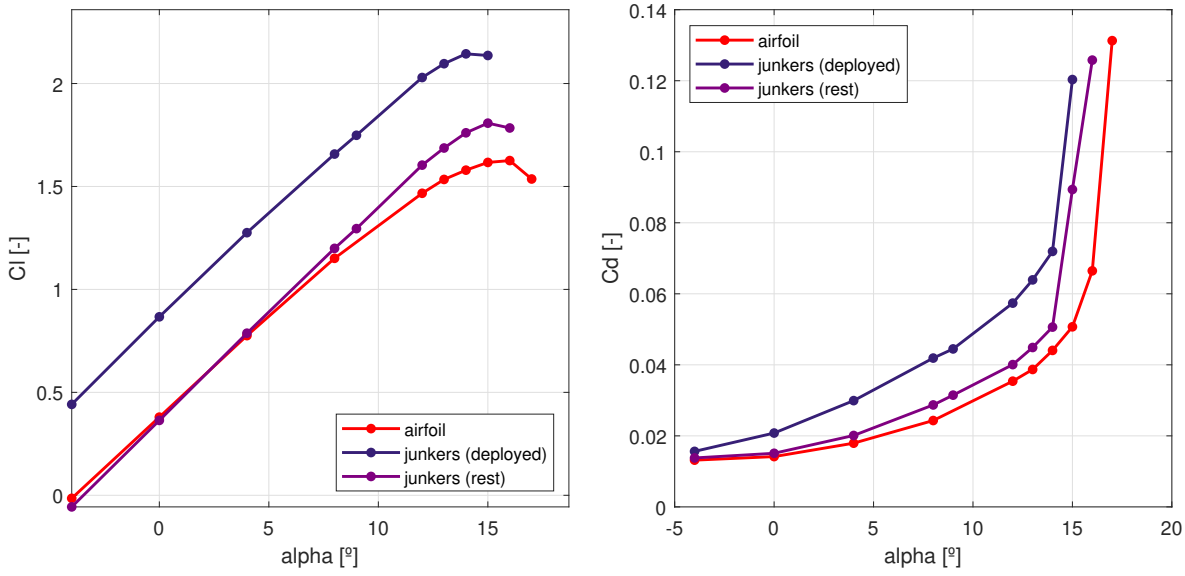
The main difference is seen in the pressure field of the flow in Figure 32. Firstly, it

can be seen that the pressure gradient extends over the entire surface, further separating the flow into a high-pressure and low-pressure region. The high-pressure region at the location of the stagnation points is also present in this case. In the distribution of the pressure coefficient in Figure 33, you can see the appearance of another curve, which identifies the surface of the flap. Positioned beyond the unit length of the airfoil, the flap essentially increases the contact area of the pressure resulting from the flow, generating an even greater force.

8.2.5 Junkers flap

In order to analyze the Junkers flap, it is necessary to evaluate both its rested and deployed versions, since the presence of the flap at rest in the lower section has an effect on the flow around the airfoil. In figure 34 the lift and drag coefficients are shown as a function of the angle of attack for the two positions of this type of flap, together with those of the clean airfoil, for comparison. It's worth noting that, like the Fowler flap, the effective area of the Junkers flap also equals 1.25, both in its retracted and extended form, since it is fixed to the airfoil and must be taken into account.

Figure 34 – (a) Lift and (b) Drag coefficients results for the clean airfoil and both positions of the Junkers flap as a function of the angle of attack.

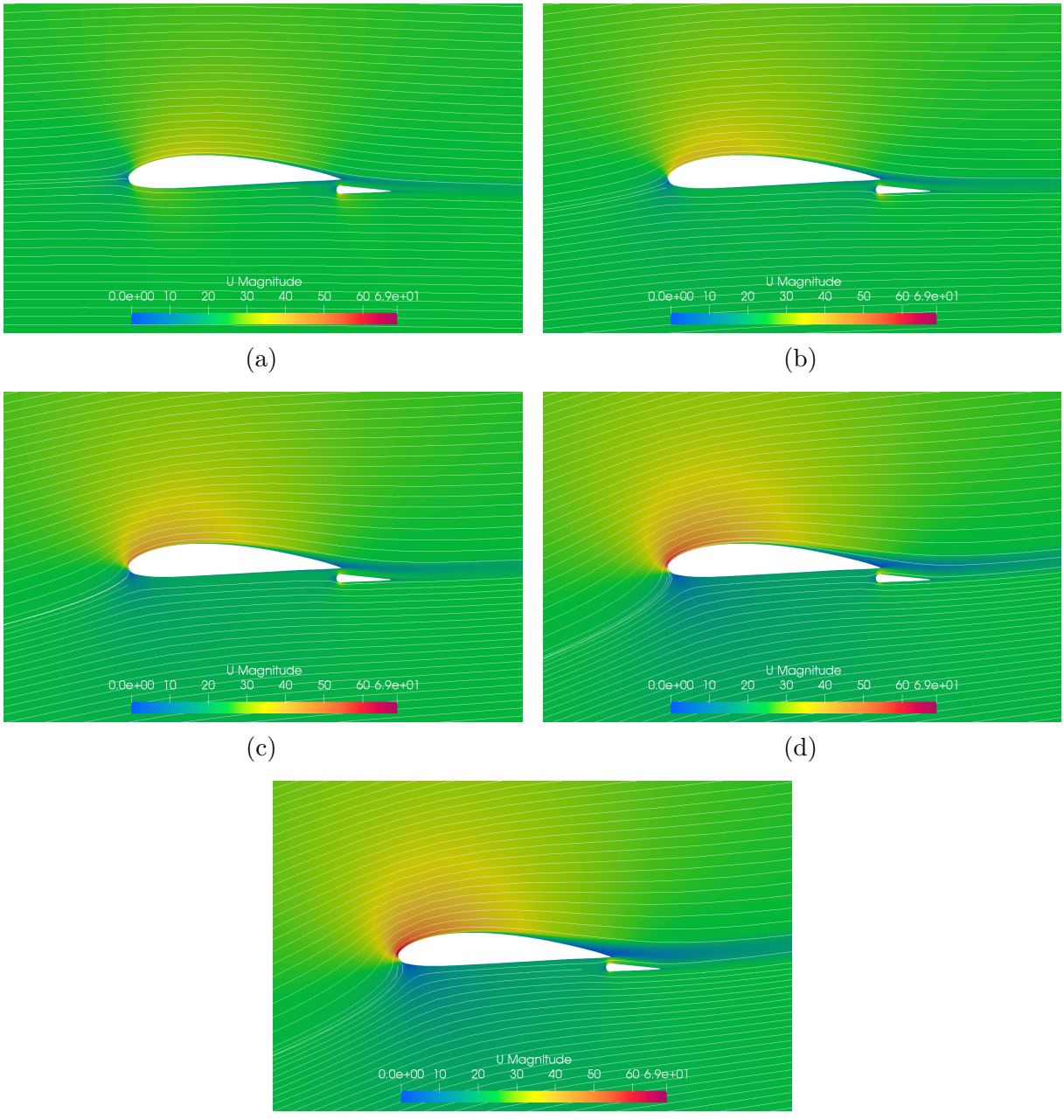


(a) (b)

The effect of the presence of the flap in the rest position is that of increasing the effective camber of the airfoil, so an intuitive consequence is that the slope of the lift curve is greater, just as was observed with the presence of other flaps. In fact, both derivatives of the lift coefficient were close, with $C_{l\alpha} = 5.856\ rad^{-1}$ for the flap at rest and $C_{l\alpha} = 5.601\ rad^{-1}$ for the extended version. When the flap is in its initial position, there is a higher maximum lift coefficient than the clean airfoil, $Cl_{max} = 1.808$, which is

achieved at a lower angle of attack, $\alpha = 15°$. The behavior of the extended flap is similar, but the deflection of the flap results in higher initial lift values even for low angles of attack, resulting in a $Cl_{max} = 2.144$ when $\alpha = 14°$. As for drag, the increase for the rest position compared to the clean airfoil is negligible.

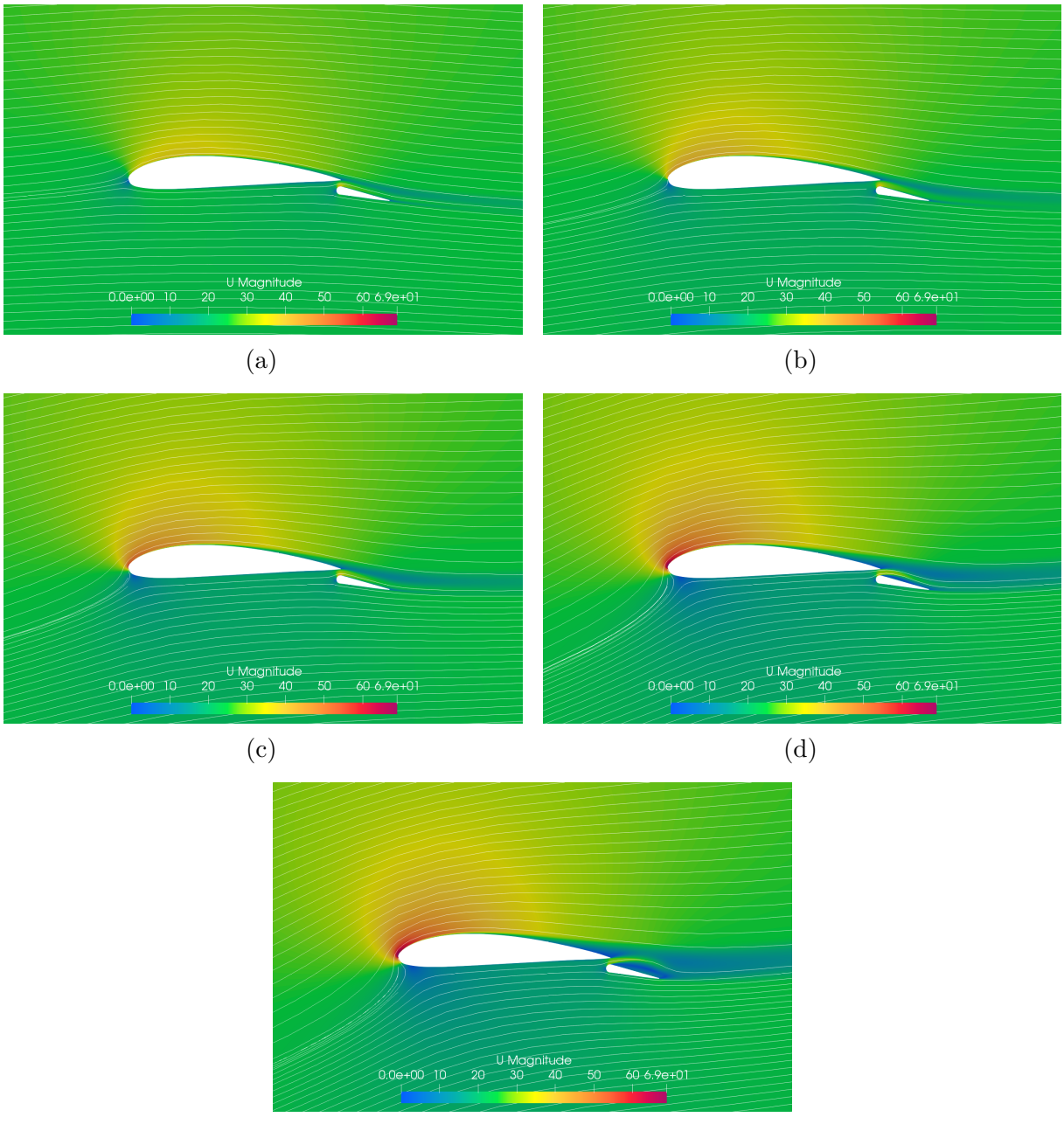
Figure 35 – Velocity field of the flow over the airfoil with Junkers flap in resting position for (a) $\alpha = 0°$, (b) $\alpha = 4°$, (c) $\alpha = 8°$, (d) $\alpha = 13°$ and (e) $\alpha = 14°$.



(a) (b) (c) (d) (e)

Figures 36 and 35 show the velocity fields and current lines of the flow around the airfoil fitted with the Junkers flap, for both the retracted and extended positions. It can be seen that, for the resting position, the flow is similar to the clean arifoil's when the AOA is low enough. As the incidence increases, the flap, even with zero deflection,

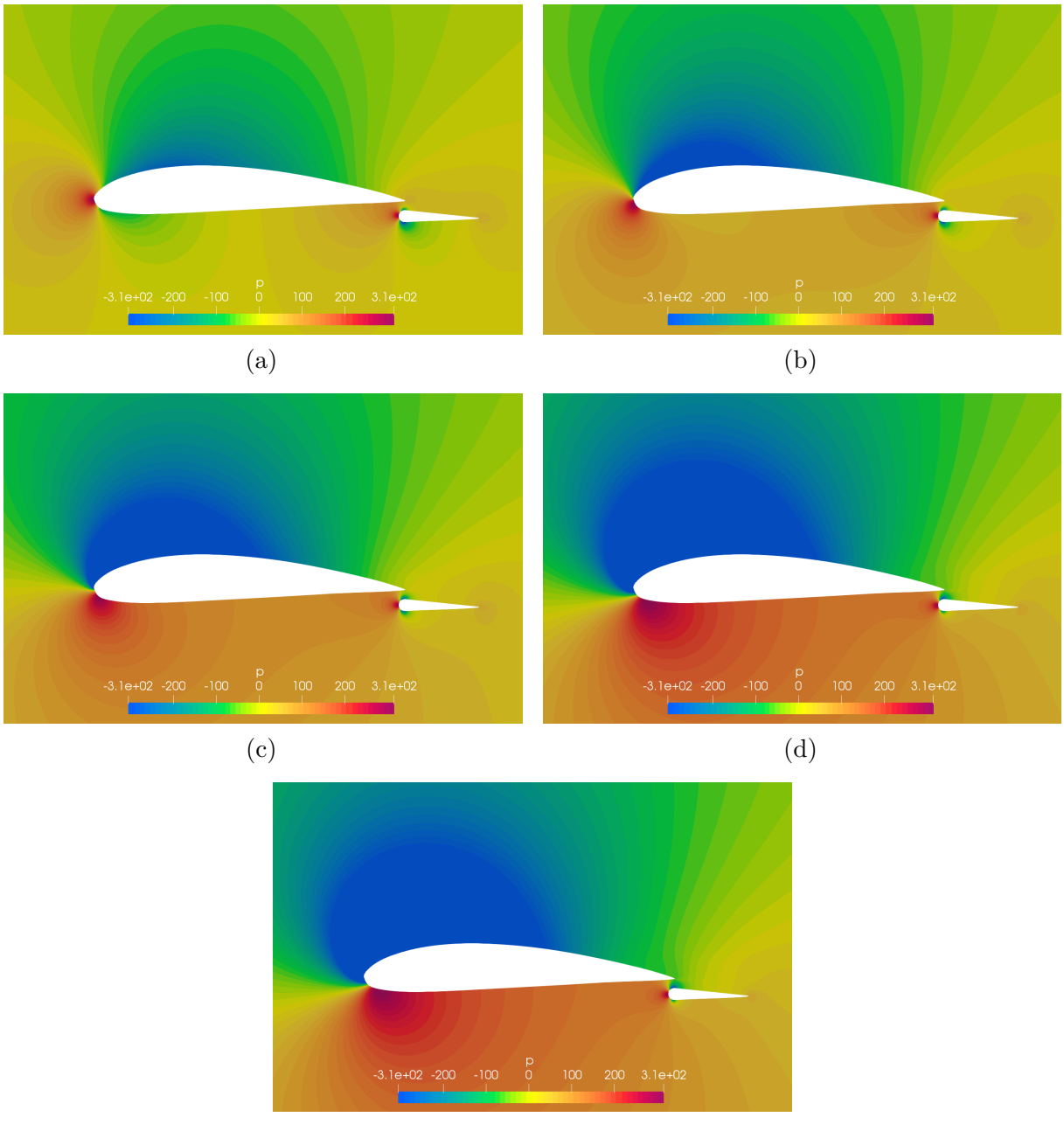
Figure 36 – Velocity field of the flow over the airfoil with Junkers flap for (a) $\alpha = 0°$, (b) $\alpha = 4°$, (c) $\alpha = 8°$, (d) $\alpha = 13°$ and (e) $\alpha = 14°$.



contributes by bending the flow, which accommodates itself to deviate from the surface.

On the other hand, when the flap is deflected at 10°, it is possible to observe a much greater deflection of the flow, which accompanies the curvature of the surface. As the angle of attack increases, it is possible to observe a common phenomenon for this type of compound airfoil: the detachment of the boundary layer does not only occur on the main element, but when $\alpha = 13°$ it is already possible to observe it happening on the flap as well. This explains the lower generation of lift at high angles compared to the Fowler flap, which kept the flow adhered to the entire surface.

Figure 37 – Kinematic pressure field of the flow over the airfoil with Junkers flap in resting position for (a) $\alpha = 0°$, (b) $\alpha = 4°$, (c) $\alpha = 8°$, (d) $\alpha = 13°$ and (e) $\alpha = 14°$.



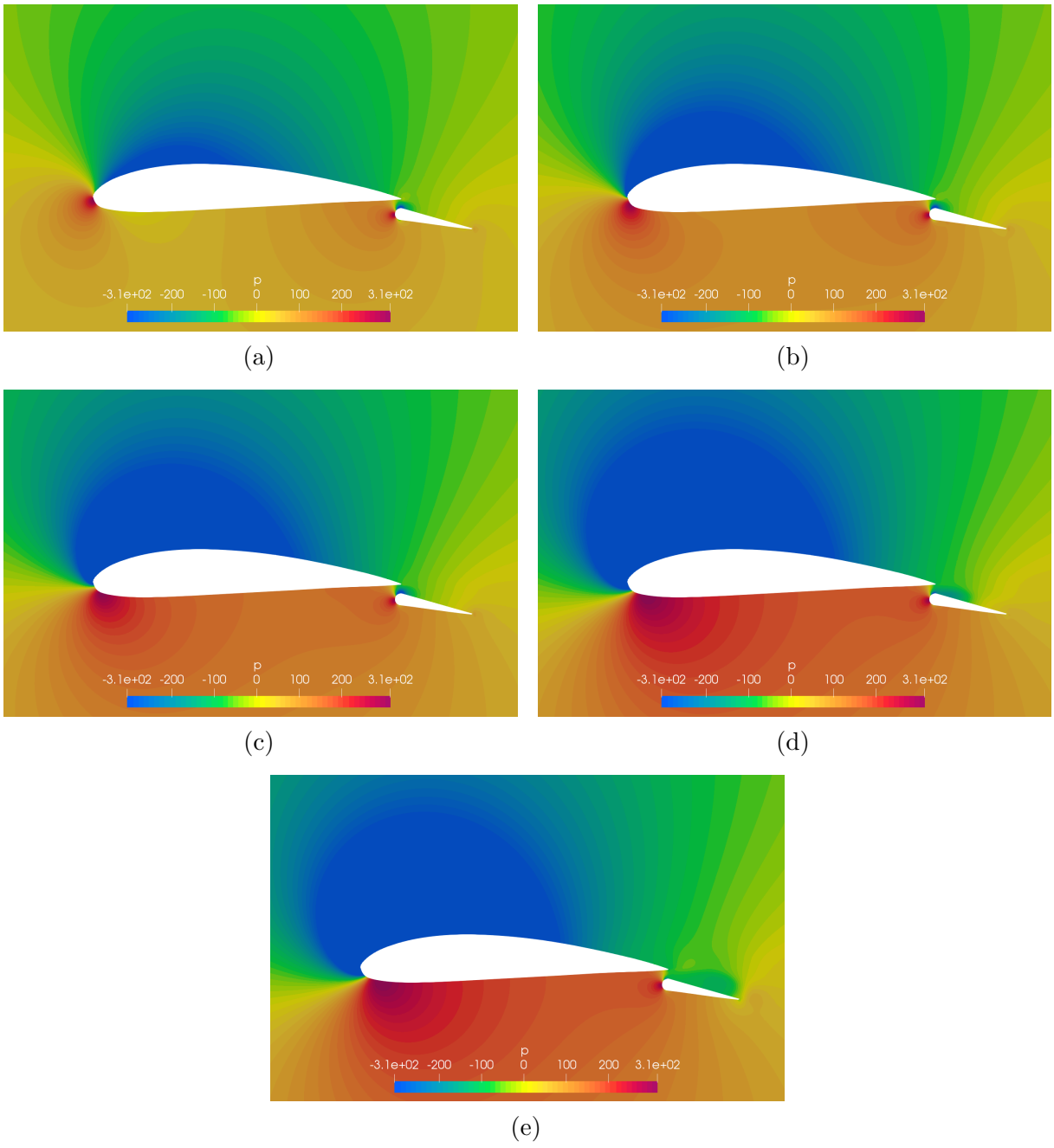
(a) (b)

(c) (d)

(e)

The pressure field shown in Figures 38 and 37 once again reinforces what was explained earlier. Similar to the Fowler flap, the flap further divides the lower high-pressure region and the upper low-pressure region when the angle of attack is greater in both flap positions. For low AOAs, the pressure difference in the flap is almost symmetrical, which indicates that its contribution to lift is low, which is why the difference to the clean airfoil is so small. However, when we analyze the extended configuration, it is possible to see a pressure difference between the lower and upper surfaces of the flap. In addition, both the negative and positive pressure gradients become more intense than in the case of flaps

Figure 38 – Kinematic pressure field of the flow over the airfoil with Junkers flap for (a) $\alpha = 0°$, (b) $\alpha = 4°$, (c) $\alpha = 8°$, (d) $\alpha = 13°$ and (e) $\alpha = 14°$.



(a) (b)

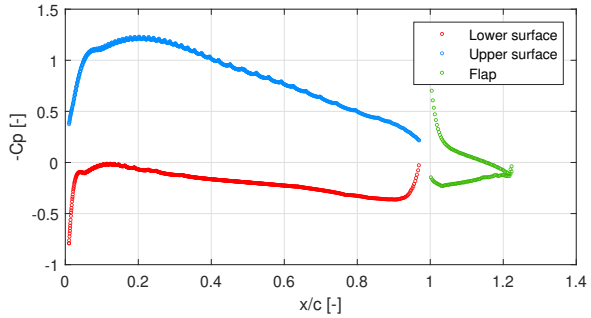
(c) (d)

(e)

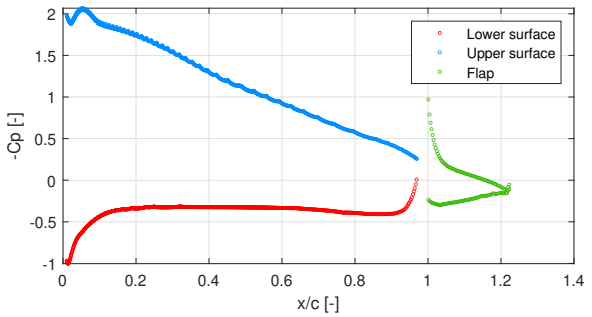
with only rotational movement (plain, split and slotted).

This latter behavior is best analyzed with the distribution of the pressure coefficient, shown in Figure 39. The behavior of the C_p is similar to that found in the Fowler flap, but the negative pressure to which the top surface of the flap is subjected decreases dramatically for angles greater than 8°, due to the separation of the boundary layer that also occurs in the flap, as noted earlier.

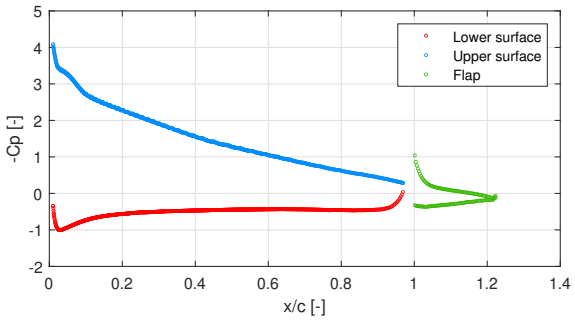
Figure 39 – Pressure coefficient distribution along the airfoil with Junkers flap for (a) $\alpha = 0°$, (b) $\alpha = 4°$, (c) $\alpha = 8°$, (d) $\alpha = 13°$ and (e) $\alpha = 14°$.



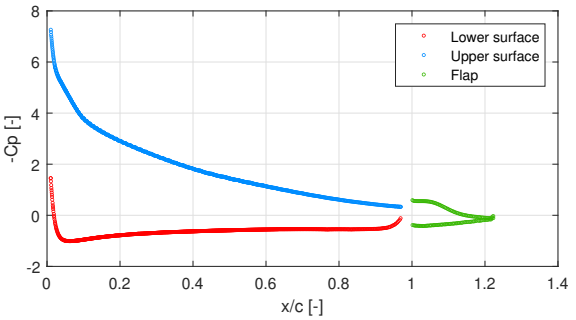
(a)



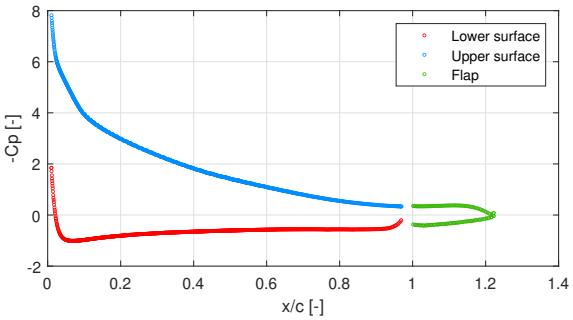
(b)



(c)



(d)



(e)

9 CONCLUSIONS

The main objective of this work was to develop and validate a robust numerical method for simulating flows around airfoils, using the OpenFOAM software, with a focus on analyzing high-lift devices under similar conditions. In addition, the work contributed to the literature by compiling these analyses, facilitating future comparisons and validations. As for the verification of results with the literature, the work presented satisfactory results, managing to replicate both experimental and numerical results with regard to the generation of lift and drag and even the distribution of pressure along the airfoil surface. The numerical validation of the mesh was also successful, which only points to the consistency of the results obtained later.

The main result of this work is the production of lift and drag for each flap configuration at different angles of attack. As previously predicted and shown in other experimental analyses, the Fowler flap proved to be the configuration with the greatest potential for generating lift, while having a small drag increment. This was followed by the Junkers flap and the slotted flap, which have very close maximum lift coefficients and modest parasite drag for moderate angles of attack. Of the three best flap configurations, the Fowler flap and the slotted flap are the most common on small and large aircraft in today's aviation industry. As for the Junkers flap, although it produces similar levels of lift to those mentioned above, it is often overlooked due to the need for a fixed structure mounted on the wing, which inevitably increases drag generation and the total weight of the aircraft.

The split flap and plain flap, on the other hand, showed the worst results of all the configurations analyzed. The former was not analyzed at its optimum deflection, which would be between 60° and 70°, so it is understandable that its performance is not among the best. But the latter, even at lower deflections, didn't provide enough lift to justify the high drag generated at even moderate angles of attack. Even so, it is understandable that both configurations are no longer widely used in aviation today.

For future work, it is suggested that numerical simulation be carried out using other turbulence models and flap deflections, but mainly using solvers that approach the problem in the transient state, and using the compressible fluid hypothesis, which is more commonly seen in aeronautical applications. In this way, the dynamics of the operation of different flap configurations will be better understood together with experimental results that the literature presents. In short, this study reinforces the importance of numerical simulation in the aeronautical industry and opens up new possibilities for the optimization of high-lift devices, contributing to significant advances in the field of aeronautical engineering.

REFERENCES

AVRAHAM, Tom. **What a DRAG...** 2024. Available from: https://cfdisraelblog.com/2024/01/19/what-a-drag-part-iii/. (accessed: 11.07.2024).

BHANDARI, Shreyas Navin. CFD Analysis of Flap of Airplane Wing Span at Subsonic Speed. **International Journal of Industrial Engineering and Technology**, 2019.

CAHILL, Jones. **Summary of section data on trailing-edge high-lift devices**. [S.l.], 1949.

FERZIGER, J.; PERIC, M. **Computational methods for fluid dynamics**. [S.l.]: Springer Science and Business Media, 2002.

FONSECA, William D. P.; REIS, Max W. F.; DIAS, Pedro F. L.; FILHO, Lourival M. S. CFD Analysis of airfoils with flaps for low Reynolds numbers. **Revista de Engenharia e Pesquisa Aplicada**, 2019.

GUDMUNDSSON, Snorri. **General Aviation Aircraft Design: Applied Methods and Procedures**. [S.l.]: Butterworth-Heinemann, 2022.

IQBAL, Muhammad Yousaf; SHAH, Syed Irtiza Ali; HASSAN, Ali; . CFD Analysis of NACA-0012 Airfoil with Various Porous Gurney Flap Geometries. **International Conference on Applied and Engineering Mathematics**, 2019.

JAWAHAR, H. Kamliya; AI, Q.; AZARPEYVAND, M.; . Experimental and numerical investigation of aerodynamic performance for airfoils with morphed trailing edges. **Renewable Energy**, 2018.

KUMAR, M. Senthil; KUMAR, K. Naveen. Design and Computational Studies on Plain Flaps. **Bonfring International Journal of Industrial Engineering and Management Science**, v. 3, 2013.

LADSON, Charles L. **Effects of Independent Variation of Mach and Reynolds Numbers on the Low-Speed Aerodynamic Characteristics of the NACA 0012 Airfoil Section**. [S.l.], 1988.

MEREDITH, P. Viscous phenomena affecting high-lift systems and suggestions for future CFD development. High-Lift System Aerodynamics. **High-Lift System Aerodynamics, AGARD CP 515**, 1993.

MONTE, Andrea Dal; CASTELLI, Marco Raciti; BENINI, Ernesto; . A Retrospective of High-Lift Device Technology. **World Academy of Science, Engineering and Technology**, 2012.

MOSER, Robert D.; KIM, John; MANSOUR, Nagi N.; . Direct numerical simulation of turbulent channel flow up to Re = 590. **American Institute of Physics**, v. 11, p. 943, 1999.

MOUKALLED, F.; MANGANI, L.; DARWISH, M.; . **The Finite Volume Method in Computational Fluid Dynamics An Advanced Introduction with OpenFOAM and Matlab**. [S.l.]: Springer, 2016.

MURAYAMA, Mitsuhiro; LEI, Zhong; MUKAI, Junichi; YAMAMOTO, Kazuomi. CFD Validation for High-Lift Devices: Three-Element Airfoil. **The Japan Society for Aeronautical and Space Sciences**, 2006.

MURAYAMA, Mitsuhiro; YAMAMOTO, Kazuomi. Numerical Simulation of High Lift Configuration using Unstructured Mesh Method. **INTERNATIONAL CONGRESS OF THE AERONAUTICAL SCIENCE**, 2004.

OPENCFD LTD. **OpenFOAM: User Guide v2112**. 2017. Available from: https://www.openfoam.com/documentation/guides/latest/doc/index.html.

REYNOLDS, Osborne. An Experimental Investigation of the Circumstances Which Determine Whether the Motion of Water Shall Be Direct or Sinuous, and of the Law of Resistance in Parallel Channels. **The Royal Society**, v. 174, p. 935–982, 1883. eprint: https://www.jstor.org/stable/109431?origin=JSTOR-pdf.

RUMSEY, Christopher. **The Spalart-Allmaras Turbulence Model**. [S.l.: s.n.], 2024. https://turbmodels.larc.nasa.gov/spalart.html [Accessed: (19/07/2024)].

ŞAHIN, I.; ACIR, A. Numerical and Experimental Investigations of Lift and Drag Performances of NACA 0015 Wind Turbine Airfoil. **International Journal of Materials, Mechanics and Manufacturing**, v. 5, 2015.

SANTOS NOGUEIRA, Rafel dos. **SIMULAÇÃO COMPUTACIONAL DO ESCOAMENTO SOBRE UM AEROFÓLIO NREL S809**. 2023. MA thesis – Universidade Federal de Uberlândia.

SARJITO; AKLIS, Nur; HARTANTO, Tri; . An optimization of Flap and Slat angle Airfoil NACA 2410 Using CFD. **An optimization of Flap and Slat angle Airfoil NACA 2410 Using CFD**, 2017.

SILVA OLIVEIRA, André da. **Low Reynolds Number Fowler Flap Design**. 2017. MA thesis – Universidade da Beira Interior.

TAN, Heyou. **CFD Analysis of a Wind Turbine Airfoil with Flap**. 2020. MA thesis – James McKelvey School of Engineering.

UNDE, Sanket S.; SUTAR, Kailasnath B. CFD Analysis of Wind Turbine Airfoil. **Journal of Emerging Technologies and Innovative Research**, v. 5, 2018.

VAN DAM, C.P. The aerodynamic design of multi-element high-lift systems for transport airplanes. **Progress in Aerospace Sciences**, 2002.

VON KARMAN, Th. **MECHANICAL SIMILITUDE AND TURBULENCE**. [S.l.], 1931.